Ion-exchangeable semiconductor materials for visible light-induced photocatalysis

Xu Zong, Lianzhou Wang*

ARC Centre of Excellence for Functional Nanomaterials, School of Chemical Engineering and AIBN, The University of Queensland, Qld 4072, Australia

*To whom corresponding author should be addressed.

Tel: +61 7 3365218, Fax: +61 7 33654199, E-mail: l.wang@uq.edu.au

Abstract: The use of semiconductor materials for solar fuel production and environmental remediation has attracted increasing attention in the past decades due to their potential to address important energy and environmental problems. Ion-exchangeable semiconductor materials represent one family of promising materials due to their unique crystal structures and structure-related photocatalytic activity. However, most of the ion-exchangeable semiconductor materials can only absorb UV light due to their wide band-gap. To efficiently utilize solar energy, it is dispensable to develop visible light-responsive semiconductor materials which can absorb solar electromagnetic irradiation accounting for almost half of the solar energy reaching the Earth's surface. In this review article, we summarize the recent advances on ion-exchangeable semiconductor materials as visible light-responsive photocatalysts with particular focus on the band-gap engineering strategies and their photocatalytic applications.

This is a post-print version of the following article: Zong, Xu and Wang, Lianzhou (2014) Ion-exchangeable semiconductor materials for visible light-induced photocatalysis. Journal of Photochemistry and Photobiology C: Photochemistry Reviews, 18 : 32-49.

Keywords: Ion-exchangeable semiconductor, Band-gap Engineering, Visible light-responsive, Photocatalysis, Water splitting

Contents

1. Introduction

1.1 Background and basic mechanism of photocatalysis

The increasing concern over the depletion of traditional fossil fuels and the serious environmental problems has re-triggered the passion on the utilization of solar energy at the turn of the new century. The main fascinating features afforded by solar energy are its abundance and cleanness. It is estimated that the magnitude of the available solar energy striking the earth's surface in 1 h (4.3×10^{20} J) is even higher than that consumed on the planet in 1 year (4.1×10^{20} J in 2001) [1]. Therefore, the capability of harvesting solar energy through a sustainable and cost-effective manner offers an ideal approach to satisfy the human's demand for renewable energy [2,3]. However, the huge

gap between the actual utilization of solar energy and its enormous theoretical potential defines a compelling imperative for the development of credible avenue for the utilization of solar energy.

The conversion of solar energy via photocatalytic reactions that occur on the surface of semiconductor materials has been extensively investigated ever since the pioneer work of Fujishima and Honda on using TiO_2 photoanode for photochemical water splitting [4]. Up to now, several approaches such as photocatalytic and photoelectrochemical water splitting, solar cells, et al. have been proposed and developed to deposit solar energy into different energy forms such as H_2 fuel and electricity. Moreover, photocatalysis has been considered as a promising approach for the sustainable organic pollutants decomposition in water and air, which has been already used in some practical applications [5].

Regardless of the different reactions occur on the semiconductor surface, the basic mechanism for all the above-mentioned photocatalytic reactions is essentially the same. Fundamentally, photocatalytic reactions involve the following steps shown in **Fig. 1**. 1) Light energy is absorbed by the photocatalyst. If the incident light energy is equivalent to or higher than the band-gap of the semiconductor, electrons can receive energy from the photons and are excited from the valence band to the conduction band, leaving free holes in the valence band. 2) The photo-generated electrons and holes (charge carriers) may recombine either in bulk or on surface of semiconductor within a very short time, releasing energy in the form of heat or photons. However, if the electrons and holes are lucky enough, they could migrate to the surfaces of the semiconductor particles. 3) The free electrons can subsequently undergo reduction reactions with electron acceptors adsorbed by the surface of semiconductor, whereas the holes can directly oxidize

adsorbed molecules or react with surface hydroxyl groups to produce hydroxyl radicals which are strong oxidizing agents. These oxidation and reduction processes together with some subsequent secondary reactions are the basic mechanisms of photocatalytic process, which underpin the development of a number of very important photocatalytic applications including organic pollutant decomposition (oxidation process by holes) for water and air purifications, water splitting and CO_2 conversion.

1.2 Ion-exchangeable semiconductor materials

As semiconductor materials are the most important component in a photocatalytic system, the development of cost-effective, non-toxic, and highly stable semiconductor materials has been the focus of investigation. Up to now, different material systems, such as oxide, sulfide, phosphide, nitride, oxynitride, oxysulfide have been developed for the conversion of solar energy [6]. Among all the materials under investigation, ion-exchangeable materials are of great interest due to their unique crystal structures and attractive photocatalytic performance.

Generally, there are two types of ion-exchangeable materials, oxide and hydroxide materials. **Fig. 2a** shows the schematic crystal structure of $Cs_{0.68}Ti_{1.83}O_4$ oxide. This representative material is typical of a lepidocrocite-type layered structure. Two layers of the network of TiO_6 octahedra sharing four edges are nested into a zigzag sheet as the structure unit of the layered titanate, and the zigzag sheets are separated by Cs^+ or hydrated proton as interlayer counter-ions. **Fig. 2b** shows the schematic crystal structure of brucite-like Layered Double Hydroxide (LDH) materials. LDH materials are composed of positively-charged layers as the building block. The layers consist of two kinds of metals that typically have +2, +3, or +4 oxidation states, octahedrally

surrounded by oxo bridges and hydroxyl groups. Negatively-charged anions are located in the inter-gallery to compensate for the excess charges of the building layers. One of the most interesting features of these two types of materials is their exchangeable nature of the interlayer cations or anions, which facilitates the incorporation of functional foreign ions into the materials. More interestingly, through well-developed intercalation-exfoliation, appreciable number of these materials can be exfoliated into single-layer two-dimensional (2D) nanosheets, which can act as versatile building blocks for electronic, magnetic, optical, photochemical, and catalytic devices [7-15]. This potential application of 2D nanosheets is evident from the tremendous research efforts on graphene and graphene-based materials in recent years.

Regarding photocatalytic applications, a large number of Ti-based ion-exchangeable oxide semiconductor materials have been investigated. Kudo et al. studied a series of cesium titanates with various Cs to Ti ratios and found $Cs_2Ti_2O_5$ with the five-coordinate structure showed higher photocatalytic activity for H_2 evolution from aqueous methanol solution than $Cs_2Ti_5O_{11}$ and $Cs_2Ti_6O_{13}$ with six-coordinate structures under UV irradiation [16]. Inoue et al. studied a series of alkali-metal titanates with a chemical formula of $M_2Ti_nO_{2n+1}$ (M = Na, K, Rb, and n = 2, 3, 4, 6) and found that a close relationship exists between the ability of produce photoexcited charges and photocatalytic activity [17]. Domen et al. investigated a series of photocatalysts with chemical formula of $M_2La_2Ti_3O_{10}$ (M = K, Rb, Cs) and found these materials were active for overall water splitting [18,19]. Moreover, the activity can be doubled if $K_2La_2Ti_3O_{10}$ was synthesized with a polymerized complex method instead of conventional solid state reaction method. Onishi et al. investigated a series of layered titanates such as $Na_2Ti_3O_7$, $K_2Ti_2O_5$, $K_2Ti_4O_9$, and $K_2Ti_6O_{13}$ and found that these

materials were active for photocatalytic H_2 evolution from aqueous methanol solutions [20]. Besides the extensive investigation on Ti-based ion-exchangeable semiconductor materials, a large number of Nb and Ta-based ion-exchangeable materials such as $A_4Nb_6O_{17}$ (A = K, Rb), A ($M_{n-1}Nb_nO_{3n+1}$) (A = Na, K, Rb, Cs; M = Ca, Sr, La), $MLnTa_2O_7$ (M = Rb, Cs, Na, H; Ln = La, Pr, Nd, Sm), $K_2LnTa_5O_{15}$ (Ln = La, Pr, Nd, Sm, Gd, Tb, Dy, Tm, Ce, Eu, Yb), $MCa_2Ta_3O_{10}$ (M = Cs, Rb, K, Na, Li) have been also developed for photocatalytic reactions [21-30].

One special feature of ion-exchangeable materials related with photocatalysis is their spatially-separately photocatalytic oxidative and reductive reaction sites. Takata et al. investigated a series of ion-exchangeable layered perovskite type materials with high efficiency for overall water splitting reactions [18]. They proposed that O_2 evolution occurred at the interlayer space of the layered materials while H_2 evolution occurred on the Ni particles at the external surface. Matsumoto et al. investigated the photodeposition of several metal and metal oxides including Ag, Cu, Cu_2O and MnO_2 on TiO_x nanosheets with the aim of directly observing the oxidative and reductive sites on the TiO_x nanosheets [31]. In their study, photoreduction depositions of Ag, Cu, and Cu_2O were found occur mainly at edges in the lateral direction of the nanosheets, indicating that the photogenerated electron mainly reacts at the edge of the nanosheets. On the other hand, photooxidation deposition of MnO_2 occurred on all over the surface of the nanosheets, indicating that the photogenerated hole reacts on all over the surface (**Fig. 3**). The spatially-separated photocatalytic oxidation and reduction reaction sites will retard the recombination of photogenerated electron-holes and will lead to high photocatalytic performance, which has been verified by the most active UV-responsive La-doped $NaTaO_3$ photocatalyst [32]. Therefore, the unique structure of

ion-exchangeable layered materials will impart beneficial feature toward efficient photocatalytic reactions.

1.3 Band-gap engineering of semiconductor materials

Although ion-exchangeable materials demonstrated attractive properties in terms of photocatalytic reaction, most of these materials are characteristic of wide band-gap. This is undesirable for the practical application as these materials can only utilize the UV light that accounts for a small fraction (3-5%) of the solar spectrum. As the absorption property (band-gap) of semiconductor materials pre-determines the up-limit of solar energy conversion efficiency of the semiconductor material system [33], the band-gap engineering of semiconductor materials to extend the light absorption of semiconductor materials toward visible region (*ca.* 46% of the solar spectrum) is highly desirable. In fact, the development of visible light-responsive semiconductor materials has been one of the hottest topics in the field of solar energy conversion scheme in the past decade.

Generally, three strategies have been used to develop visible light-responsive semiconductor materials. To make these strategies legible, we will use the challenging water splitting reactions as a demonstration (**Fig. 4**). The first strategy (A) is to find materials that have suitable valence band and/or conduction band levels and small band-gap for overall or half water splitting reactions under visible light. Different types of visible light responsive semiconductor materials such as oxide, nitride, oxynitride, sulfide, and oxysulfide materials have been developed in recent years [6, 34-43]. The second strategy (B) is to dope foreign elements into the crystal lattice of active photocatalysts to form donor or acceptor levels in the band-gap. For example, metal

doping, non-metal doping, and metal/non-metal co-doping have been widely used to induce visible light absorption in wide band semiconductor materials including the benchmark TiO_2 photocatalyst [44-56]. In some cases, the dopants in the lattice may also form new energy band instead of doping level in the band-gap of the materials. And the last strategy (C) is to couple wide band-gap semiconductor materials with narrow band-gap semiconductor materials or organic dye. Although, wide band materials cannot absorb visible light, they can be "sensitized" by the narrow band-gap semiconductor materials (organic dye), and therefore the composite system can absorb visible light [57-60]. In many cases, due to the strong coupling effect between the wide band-gap and small band-gap (organic dye) materials and proper band alignment, higher performance has been observed in the composite material system than that in a single component system.

1.4 Scope of this review article

In recent years, owing to the increasing interest in renewable solar energy conversion and utilization, many important progresses have been made in this photocatalysis field and several excellent reviews has been published [6, 61-69]. However, there are still no reviews focusing on ion-exchangeable semiconductor materials that are active under visible light irradiation. Considering the unique crystal structures of this type of materials and the attractive photocatalytic performance, here we provide an overview of the recent advances in the development of visible light-responsive ion-exchangeable semiconductor materials for solar H_2 generation and environmental remediation, with particular focus on the band-gap engineering strategies. Only the representative results in the past decade will be detailed and therefore this review is not meant to be wholly thorough.

2. Ion-exchangeable materials for visible light-induced photocatalysis

2.1 Pristine visible light-responsive ion-exchangeable materials

Most of the ion-exchangeable materials are wide band-gap oxide or hydroxide materials. Up to now, only few ion-exchangeable oxide materials have been reported to show visible light-induced photocatalytic activity. For ion-exchangeable hydroxide materials, more visible light-responsive candidates are available due to the flexible compositions of the building block layer.

Yoshimura et al. reported a layered niobate, $RbPb_2Nb_3O_{10}$, which exhibited strong absorption in the visible light region [70]. **Fig. 5** shows the schematic crystal structure of $RbPb_2Nb_3O_{10}$. $RbPb_2Nb_3O_{10}$ is composed of perovskite $Pb_2Nb_3O_{10}$ layer with the intercalation of Rb^+ between the layers and the interlayer Rb^+ can be exchanged with other cations. $RbPb_2Nb_3O_{10}$ was prepared with a solid state reaction method from the mixture of Rb_2CO_3, PbO and Nb_2O_5 at 1273 K for 2 days with intermediate grinding. 10% excess of Rb_2CO_3 was added to compensate the loss due to its volatilization at high temperatures. The as-prepared $RbPb_2Nb_3O_{10}$ showed strong absorption in wavelength up to *ca.* 500 nm and weaker tail-like absorption in longer wavelength region. On the contrary, $RbCa_2Nb_3O_{10}$ with similar structure only showed absorption in the UV region. It was reported that orbitals of Pb 6s in Pb^{2+} can form valence bands above the valence band consisting of O 2p orbitals and lead to smaller band-gaps. Therefore, the strong band-to-band absorption observed on $RbPb_2Nb_3O_{10}$ should be ascribed to the participation of Pb^{2+} in the formation of the band structures of $RbPb_2Nb_3O_{10}$. The role of Pb^{2+} orbitals for narrowing the band-gap of semiconductor materials have been also observed in other material systems [71,72]. Under visible light irradiation ($\lambda > 420$ nm),

$RbPb_2Nb_3O_{10}$ showed activity for photocatalytic H_2 production from aqueous methanol solution when loaded with Pt as cocatalyst and O_2 production from $AgNO_3$ aqueous solution. However, the activity achieved on $RbPb_2Nb_3O_{10}$ is extremely low. Then Rb^+ in the interlayer was exchanged with H^+ by treating $RbPb_2Nb_3O_{10}$ in HNO_3 at room temperature to obtain the corresponding material with a chemical formula of $HPb_2Nb_3O_{10}$. The as-obtained $HPb_2Nb_3O_{10}$ demonstrated drastically enhanced activity for photocatalytic H_2 evolution under similar reaction conditions. It is suggested that $HPb_2Nb_3O_{10}$ is easily hydrated under ambient conditions while $RbPb_2Nb_3O_{10}$ is not hydrated even in an aqueous solution. The interlayer spacing of $HPb_2Nb_3O_{10}$ increased upon hydration, which facilitated the migration of reactant into the interlayer space of $HPb_2Nb_3O_{10}$. Therefore, $HPb_2Nb_3O_{10}$ showed much higher activity than $RbPb_2Nb_3O_{10}$. It was also found that the source of Pt had drastic influence on the photocatalytic activity of $HPb_2Nb_3O_{10}$.When $[Pt(NH_3)_4]Cl_2$ was used instead of H_2PtCl_6 as the Pt source, much higher H_2 photocatalytic activity was obtained. As shown in **Fig. 6**, $PtCl_6^{2-}$ is not able to intercalate into the interlayer space due to its anionic nature. Therefore, Pt cocatalyst is just deposited on the external surface of $HPb_2Nb_3O_{10}$. On the contrary, $[Pt(NH_3)_4]^{2+}$ with cationic nature can intercalate into the interlay space through ion-exchange reaction with protons and then be reduced into ultrafine Pt catalyst in the interlayer space. These Pt particles in the interlayer space are expected to work as efficient catalytic sites for H_2 evolution. Therefore, much higher photocatalytic activity was obtained when $[Pt(NH_3)_4]Cl_2$ was used as the Pt source. These interesting findings demonstrated the drastic influence of the unique structures of ion-exchangeable materials on the modification of their photocatalytic properties, which has not been observed on common semiconductor materials.

Silva et al. reported a series of LDH for visible light-induced oxygen generation from photocatalytic water splitting process in 2009 [73]. Zn/Ti, Zn/Ce, and Zn/Cr LDH with different Zn/metal atomic ratios were prepared using two methods. A co-precipitation of metal salts from aqueous solution with NaOH solution was used for the preparation of (Zn/Cr/Al) LDH materials. As LDH materials with M^{II}/M^{III} atomic ratio of two have high crystallinity, Al^{3+} was added during the synthesis to maintain the $Zn^{2+}/ (Cr^{3+}+Al^{3+})$ atomic ratio at 2:1. (Zn/Cr/Al) LDH materials with Zn/Cr atomic ration of 4:1.75, 4:1, and 4:0.25 were prepared. To prepare Zn/Ti or Zn/Ce LDH materials, tetravalent elements (Ti^{4+}, Ce^{4+}) will co-precipitate with Zn^{2+} through continuous release of ammonia by urea decomposition in water at moderate temperatures. **Fig. 7** shows the UV-Vis spectra of the as-prepared LDH materials. (Zn/Ti) LDH and (Zn/Ce) LDH materials showed absorption edges at 350 and 400 nm, while (Zn/Cr) LDH showed two absorption peaks in the visible region which are ascribed to ligand to metal transitions in octahedral Cr ions. Under visible light irradiation (λ >420 nm) and in the presence of $AgNO_3$ as the sacrificial reagents, quantum efficiency values of 15.1%, 37.8%, and 60.9% were reported for (Zn/Ti), (Zn/Ce), (Zn/Cr) LDH, respectively. Considering the poor (or even no) visible light absorption of (Zn/Ti) and (Zn/Ce) LDH and the absorption nature of the (Zn/Cr) LDH, the efficiency achieved in this study is quite high. Using similar approach, Lee et al. synthesized several new titanium-embedded LDH such as (Ni/Ti) LDH and (Cu/Ti) LDH [74]. The as-prepared materials also showed absorption in the visible region and photocatalytic activity for O_2 production under visible light irradiation.

Parida et al. reported the preparation of carbonate-intercalated Zn/Cr LDH and its photocatalytic activity for H_2 production under visible light [75]. Carbonate-intercalated

Zn/Cr LDH was prepared by a co-precipitation method similar with that of preparing Zn/Cr LDH. However, sodium carbonate was used together with sodium hydroxide to intercalate carbonate in the interlayer of the material during the synthesis. The as-prepared material exhibited light absorption in the visible region and photocatalytic activity for H_2 generation from aqueous methanol solution under visible light irradiation. The Zn/Cr – CO_3 LDH showed enhanced photocatalytic activities compared to Zn/Cr LDH due to the facile reaction between carbonate ions and photogenerated holes to generate intermediate carbonate radicals, which can inhibit the rapid recombination of photogenerated electrons and holes. Parida et al. also reported the preparation of Zn/Fe LDHs with different intercalated anions with co-precipitation method [76]. The as-prepared LDHs showed visible-light absorption and higher photocatalytic activity for degradation of azo dyes compared to commercial ZnO and Fe_2O_3 under solar light irradiation. Several types of LDH materials with visible light response were also reported recently for environmental remediation or solar fuel production under visible light [77,78].

2.2 Doping of non-metal elements in ion-exchangeable materials

Non-metal doping especially Nitrogen (N) doping has been demonstrated to be an effective strategy to inducing visible light absorption to wide band-gap semiconductor materials [44]. For example, N doping has been widely used to modify the electronic structures of TiO_2 to achieve functionality under visible light irradiation. Up to now, two main hypotheses have been proposed, namely that (i) the up-shifted valence band maximum by N 2p states and/or (ii) the localized states from N 2p states as well as concomitant colour centres in the band-gap are considered as the origin of visible light

absorption. Although there is still debate on the origin of visible light absorption induced by the N doping, N doping has been testified to be an effective strategy for the development of new types of TiO_2 photocatalysts. Wang et al. have successfully extended this strategy to a series of wide band-gap ion-exchangeable materials and systematically investigated the influence of anion doping on the band structure, light absorption as well as the visible light-induced photocatalytic activity of these ion-exchangeable materials [79-88].

The first reported anion-doped ion-exchangeable materials are N-doped $Cs_{0.68}Ti_{1.83}O_4$ and $H_{0.68}Ti_{1.83}O_4$ [79]. The schematic structure of $Cs_{0.68}Ti_{1.83}O_4$ and $H_{0.68}Ti_{1.83}O_4$ is shown in **Fig. 2**. $Cs_{0.68}Ti_{1.83}O_4$ was typically prepared with a solid state reaction method. N doping in $Cs_{0.68}Ti_{1.83}O_4$ was then achieved by heating $Cs_{0.68}Ti_{1.83}O_4$ at 1023 K in flowing ammonia gas. The resulting $Cs_{0.68}Ti_{1.83}O_{4-x}N_x$ was finally treated in HCl solution to exchange the interlayer Cs^+ with protons to obtain $H_{0.68}Ti_{1.83}O_{4-x}N_x$. After N doping, the white colour $Cs_{0.68}Ti_{1.83}O_4$ changed to yellow $H_{0.68}Ti_{1.83}O_{4-x}N_x$, indicating the drastic modification of the N doping on the band structures of the pristine $Cs_{0.68}Ti_{1.83}O_4$. This modification was clearly demonstrated in the UV-Vis light absorption spectra of the materials shown in **Fig. 8**. In contrast to the pristine $Cs_{0.68}Ti_{1.83}O_4$ and $H_{0.68}Ti_{1.83}O_4$, the absorbance band edge of $Cs_{0.68}Ti_{1.83}O_{4-x}N_x$ and $H_{0.68}Ti_{1.83}O_{4-x}N_x$ exhibited an extraordinary red shift from 356 and 380 nm to 472 and 453 nm, respectively. Moreover, $Cs_{0.68}Ti_{1.83}O_{4-x}N_x$ and $H_{0.68}Ti_{1.83}O_{4-x}N_x$ showed band-to-band absorption feature, which are quite different from the weak tail-like absorption commonly observed in N-doped TiO_2. This feature is ascribed to the homogeneous doping of N in $Cs_{0.68}Ti_{1.83}O_{4-x}N_x$, which was confirmed by XPS and TEM analysis. Density functional theory (DFT) calculations indicated that the valence band

of $Cs_{0.68}Ti_{1.83}O_{4-x}N_x$ and $H_{0.68}Ti_{1.83}O_{4-x}N_x$ were mainly spanned by O_{2p} and mixed with N_{2p} orbitals, while those of the undoped ones were dominated by O_{2p} orbital. The participation of N_{2p} orbitals in the formation of valence band results in the up-shift of the valence band and led to drastically decreased band-gaps. The photocatalytic performance of $Cs_{0.68}Ti_{1.83}O_{4-x}N_x$ and $H_{0.68}Ti_{1.83}O_{4-x}N_x$ was then tested by the degradation of Rhodamine G under visible light irradiation ($\lambda > 420$ nm). It was found that $Cs_{0.68}Ti_{1.83}O_{4-x}N_x$ with smaller specific surface area showed better performance than N-doped P25 titania. Moreover, $H_{0.68}Ti_{1.83}O_{4-x}N_x$ showed even better activity than $Cs_{0.68}Ti_{1.83}O_{4-x}N_x$ due to the large specific surface area, stronger oxidative powder of the photogenerated holes and more easily accessible photocatalytic reaction pathway. The observed excellent photocatalytic activities on $H_{0.68}Ti_{1.83}O_{4-x}N_x$ and $Cs_{0.68}Ti_{1.83}O_{4-x}N_x$ are supposed to be due to the drastic modification of the electronic structure as well as the light harvesting properties of pristine $Cs_{0.68}Ti_{1.83}O_4$ and $H_{0.68}Ti_{1.83}O_4$ by homogeneous N doping, and the homogeneous N doping is ascribed to the unique layered structure of $Cs_{0.68}Ti_{1.83}O_4$ which offers an excellent pathway for the uniform nitriding reaction and distribution of N dopant in pristine $Cs_{0.68}Ti_{1.83}O_4$. This work not only advances the fundamental understanding of the substantial role of uniform N doping in titania-based photocatalysts but also could be applied in a wide variety of other layered semiconductors materials. In the following work, by finely controlling the doping amount of N in $Cs_{0.68}Ti_{1.83}O_4$, the photocatalytic activity of $Cs_{0.68}Ti_{1.83}O_{4-x}N_x$ was rationally tuned by modifying its valence band positions. The interplay of absorbance, oxidative potential and mobility of charge carries was found to affect the photocatalytic activity of $Cs_{0.68}Ti_{1.83}O_{4-x}N_x$ [80].

One interesting feature of $H_{0.68}Ti_{1.83}O_{4-x}N_x$ is its capability to be exfoliated into N-doped single-layer titania nanosheets [81]. **Fig. 9** shows the schematic procedure of preparing N-doped $Ti_{0.91}O_2$ nanosheets with a well-developed strategy generally used for preparing oxide single-layer nanosheets [82]. N-doped $H_{0.68}Ti_{1.83}O_4$ was first prepared following a procedure mentioned above. The as-prepared $H_{0.68}Ti_{1.83}O_{4-x}N_x$ was then put in tetrabutylammonium hydroxide (TBAOH) aqueous solution and gently shaken for several days. During the shaking of the solution, large sized TBA^+ ions will gradually replace the protons in the interlayer galleries of $H_{0.68}Ti_{1.83}O_{4-x}N_x$ to expand the layered structures, finally resulting in fully exfoliated $Ti_{0.91}O_{2-x}N_x$ nanosheets with TBA^+ ions as the counter ions to stabilize them in aqueous solution. The single-layer nature of the resulting $Ti_{0.91}O_{2-x}N_x$ nanosheets was confirmed by its extremely small thickness of < 1 nm as shown by the Atomic force microscopy (AFM) image in **Fig. 10a**. More interestingly, the resulting $Ti_{0.91}O_{2-x}N_x$ nanosheets preserve the visible light absorption of the pristine $H_{0.68}Ti_{1.83}O_{4-x}N_x$, which is evident contrast with that of the corresponding white $Ti_{0.91}O_2$ nanosheets **(Fig. 10b)**. The $Ti_{0.91}O_{2-x}N_x$ nanosheets were then assembled onto ITO substrate using a layer-by-layer self-assembly technique. The resulting film consisted of PEI-$Ti_{0.91}O_{2-x}N_x$ nanosheets exhibited an enhancement of photocurrent compared to that of undoped nanosheets under visible light irradiation. This non-metal doping strategy can be easily extended to a large number of layered metal oxide compounds that have the characteristics of intercalation-exfoliation behaviour. Moreover, the exfoliated $Ti_{0.91}O_{2-x}N_x$ nanosheets can be used as the building blocks for the fabrication of potential electronic and optoelectronic devices [83,84].

The concept of homogeneous anion doping to induce strong band-to-band visible light absorption was then successfully applied to several semiconductor materials with

unique ion-exchangeable property. Mukherji et al. investigated the effect of N doping in $CsTaWO_6$ for photocatalytic H_2 production under solar irradiation [85]. N-doped $CsTaWO_6$ is composed of $[Ta/W]O_6$ octahedra and has a defect pyrochlore structure as show in **Fig. 11**. It was prepared with a solid state reaction by heating a mixture of Cs_2CO_3, Ta_2O_5, and WO_3. N doping in $CsTaWO_6$ was achieved by heating $CsTaWO_6$ in ammonia flow at 783 K and the amount of N dopant was tuned by varying the nitridation duration. XRD characterizations indicate that the crystal structure of $CsTaWO_6$ remains intact upon N doping. UV-Vis spectra indicate that N doping in the compound results in a red-shift of the absorption edge from 358 nm to 580 nm, corresponding to a reduced band-gap from to 3.8 to 2.3 eV. DFT calculations indicate that the significantly reduced band-gap of $CsTaWO_6$ upon N doping is due to the mixing of N 2p and O 2p orbital, and N 2p orbitals mainly contribute to the formation of the top of the valence band of $CsTaWO_{6-x}N_x$. The photocatalytic performances of $CsTaWO_{6-x}N_x$ as well as $CsTaWO_6$ photocatalysts were evaluated by the photocatalytic H_2 production reaction in aqueous ethanol solution under solar irradiation. Without loading any cocatalyst, undoped $CsTaWO_6$ was found to exhibit higher activity than P25 benchmark photocatalyst. After N doping the as-prepared $CsTaWO_{6-x}N_x$ showed a nearly 100% increase in the photocatalytic activity compared with the undoped one. Moreover, $CsTaWO_{6-x}N_x$ also showed activity for H_2 production only under visible light irradiation (λ >420 nm). The high activity achieved on $CsTaWO_{6-x}N_x$ is ascribed to its significant band-to-band absorption due the homogenous N doping facilitated by the open structure of pristine $CsTaWO_6$. In the following study, the protonated form of $CsTaWO_{6-x}N_x$, $HTaWO_{6-x}N_x$, was obtained by treating $CsTaWO_{6-x}N_x$ in HNO_3. Improved visible light absorption on $HTaWO_{6-x}N_x$ was confirmed by combining

experimental and theoretical investigations [86]. $CsTaWO_6$ was also tentatively doped with different anion elements such as sulfur in order to modify its properties by expanding the homogeneous doping strategy to a wide range of doping elements [87]. Improved light absorption and enhanced photocatalytic activity was also observed on $CsTaWO_6$ after sulfur doping and S/N co-doping.

The $H_{0.68}Ti_{1.83}O_{4-x}N_x$ and N-$HTaWO_6$ compounds mentioned above were obtained by H^+-exchange of the Cs^+ in the inter-galleries of $Cs_{0.68}Ti_{1.83}O_{4-x}N_x$ and N- $CsTaWO_6$, respectively. Li et al. reported a different strategy of doping N into ion-exchangeable layered niobic acid (HNb_3O_8) [88]. HNb_3O_8 is composed of two-dimensional $Nb_3O_8^-$ nanosheets with corner- and edge-sharing NbO_6 octahedra building block, and the H^+ cations are located in the interlayer of $Nb_3O_8^-$ nanosheets. By heating HNb_3O_8 together with urea as the N source at proper temperature and duration, N can be doped into the lattice of HNb_3O_8 without changing the crystal structure of the pristine HNb_3O_8. However, when HNb_3O_8 was treated in flowing ammonia, N cannot be doped at low temperature, while high temperature treatment in NH_3 will destroy the original structure of HNb_3O_8. Therefore, urea plays a unique role in introducing N dopant into the lattice of HNb_3O_8 at lower temperatures. The doping of N was found to impart visible light absorption to the resulting N-HNb_3O_8, which was not observed in the pristine HNb_3O_8 (**Fig. 12**). Under visible light irradiation (λ >420 nm), the as-prepared N-HNb_3O_8 showed superior activity for the degradation of RhB than N-doped Nb_2O_5 and N-doped TiO_2 samples. The favourable properties in N-HNb_3O_8 such as layered structure, the light absorption characteristic, and the protonic acidity were supposed to be the reason for the high activity observed. In the following work, Li et al. extended this strategy to

dope N into another layered titanic acid, $H_2Ti_4O_9$. Enhanced visible light absorption and corresponding photocatalytic activity were also observed in N-$H_2Ti_4O_9$ [89].

Anion doping was also found to impart other functionality to ion-exchangeable materials. Recently we reported an N-doped ion-exchangeable layered tantalate, N-$CsCa_2Ta_3O_{10}$, for photocatalytic water oxidation reactions [90]. **Fig. 13** shows the schematic crystal structure of N-$CsCa_2Ta_3O_{10}$ due to the partial substitutional N doping for O in the crystal lattice. N-$CsCa_2Ta_3O_{10}$ was prepared by heating pristine $CsCa_2Ta_3O_{10}$ in ammonia flow. It preserves the crystal structure of the pristine $CsCa_2Ta_3O_{10}$ after N doping, and the colour of N-$CsCa_2Ta_3O_{10}$ ranges from pale yellow to red with increasing nitridation temperature, which is in great contrast with the white colour of the pristine $CsCa_2Ta_3O_{10}$. DFT calculations indicated that after the substitutional N doping, the valence band of N-$CsCa_2Ta_3O_{10}$ was spanned by O2p and N2p, which leads to a substantial narrowing of the band-gap from 2.07 to 1.55 eV for undoped and N-doped samples, respectively, and the contribution of N to the top of the valence band is expected to play an important role in extending the absorption of the N-doped samples into the visible region. Under visible light irradiation, N-$CsCa_2Ta_3O_{10}$ showed high photocatalytic activity for the water oxidation reaction, and the sample prepared at moderate conditions showed the optimum performance. This work presents a novel type of ion-exchangeable photocatalyst capable of producing O_2 from water splitting under visible light. The N doping strategies have been also employed for the preparation of a series of N-doped ion-exchangeable materials with visible light-induced photocatalytic activities [91-95].

Following the work on N-doped $CsCa_2Ta_3O_{10}$, Ida et al. obtained calcium tantalum oxynitride $[Ca_2Ta_3O_{9.7}N_{0.2}]^-$ nanosheets via proton exchange and subsequent

intercalation processes from parent N-doped $CsCa_2Ta_3O_{10}$ [96]. The parent N-doped $CsCa_2Ta_3O_{10}$ was found to exhibit quite low activity for photocatalytic H_2 production from aqueous methanol solution under visible light. After exchanging Cs^+ to H^+, the resulting N-doped $HCa_2Ta_3O_{10}$ showed enhanced photocatalytic activity. Drastically enhanced photocatalytic activity was further achieved on $[Ca_2Ta_3O_{9.7}N_{0.2}]^-$ nanosheets loaded with Rh as cocatalyst (**Fig. 14**). Moreover, Rh-loaded $[Ca_2Ta_3O_{9.7}N_{0.2}]^-$ nanosheets also exhibited activity for H_2 and O_2 evolution from pure water under UV-light irradiation. The improved photocatalytic activity originates from the characteristics of nanosheets such as thin thickness and large surface area. This work demonstrated the potential application of oxynitride nanosheets for photocatalytic H_2 production from water.

The N doping in oxide photocatalysts such as TiO_2 can be achieved by either high temperature treatment process or wet-chemical solution methods, whereas the wet-chemically doped oxide materials are generally less stable than heat-treated samples. On the other hand, the doping of N in ion-exchangeable materials or nanosheets is generally achieved by heating the parent materials in the presence of ammonia gas (or urea) as the N dopant source and the subsequent intercalation-exfoliation treatment. N has been reported to be directly doped into oxide nanosheets at much more milder conditions. Matsumoto et al. found that the N can be doped in oxide nanosheets by irradiating the nanosheets with high energy UV light in the presence of TBAOH at room temperature (**Fig. 15)** [97]. The absorption of the oxide nanosheets in the visible region increased with the prolonged irradiation, indicating the corresponding increased N doping. It was suggested that residue TBA during the synthesis of the restacked nanosheets assembly acted as the N doping source during the irradiation, and TBA^+ was

found to play a unique role in the N doping because other amines such as ethylamine, dimethylamine and trimethylamine were found to be ineffective for nitrogen doping. Among different types of nanosheets derived from $K_4Nb_6O_{17}$ (Nb-O), $KCa_2Nb_3O_{10}$ (Ca-Nb-O), $K_2Ti_4O_9$ (Ti-O), and $KTiNbO_5$ (Ti-Nb-O), the N doping occurred for Nb-O, Ca-Nb-O, and Ti-Nb-O, but did not occur for Ti-O nanosheets without Nb. Nanosheets with Nb-O chemical bond were supposed to have higher conduction band energy, which facilitate the N doping during the irradiation. Under light irradiation ($\lambda > 420$ nm), the as-prepared N-doped Nb-O nanosheets showed activity for photocatalytic H_2 production from aqueous methanol solution, while undoped Nb-O nanosheets are inactive under the same reaction condition, therefore demonstrating the effectiveness of this simple and mild strategy for doping N in oxide nanosheets.

2.3 Doping of metal elements in ion-exchangeable materials

The doping of proper metal elements into pristine semiconductor materials has been demonstrated to be an effective strategy of inducing visible light absorption in a variety of wide band-gap semiconductor materials. For ion-exchangeable materials, two pathways of doping metal ions have been used to achieve visible light absorption in the pristine materials. The first one is the exchange of alkaline ions with metal ions that can form new band in the band-gap of the pristine materials. The second one is the substitutional doping of foreign cation for the pristine cation that forms the building unit of the crystal structures. The second strategy is challenging to layered oxide materials due to the structural fragility of these materials, which usually accompanies the collapse of the original structure upon metal doping. Up to now, only few ion-exchangeable oxide nanosheet materials were reported to show light absorption in the visible region together with visible light induced photocatalytic activity upon cation doping. For

ion-exchangeable hydroxide nanosheet materials, the relatively flexible composition of the nanosheets building makes the doping of divalent or trivalent metals relatively simple.

Hosogi et al. investigated the photocatalytic activities of a series of Sn^{2+}-doped ion-exchangeable layered materials, including $KTiNbO_5$, $K_4Nb_6O_{17}$, $CsTi_2NbO_7$, $K_2Ti_4O_9$, $K_2Ti_2O_5$, and $Cs_2Ti_6O_{13}$ [98]. By stirring these layered materials in a mixed solution of HCl and $SnCl_2$, part of the alkaline metal ions in these materials was exchanged with Sn^{2+} to achieve Sn-doped compounds. The band-gap of the Sn^{2+}-exchanged layered metal oxides were 0.7-1.2 eV narrower than those of the pristine layered materials. The origin of the visible-light absorption was supposed to be due to the electronic transition from an electron donor level consisting of Sn5s orbitals to conduction bands consisting of Ti3d and Nb4d orbitals as shown in **Fig. 16a**. The participation of Sn5s orbitals for inducing visible light absorption has been reported in other material system [99]. Moreover, the potential of the electron donor level negatively shifted as the amount of ion-exchanged Sn^{2+} increased. Therefore, the valence band structures of Sn^{2+}-exchanged materials were greatly influenced by the amount of Sn^{2+} dopant (**Fig. 16b**). The Sn^{2+} -exchanged layered materials were found to exhibit activity for the photocatalytic H_2 production in aqueous method solution under visible light irradiation, and the photocatalytic activity was influenced by the type of the pristine layered materials, among all of which $Sn^{2+}/KTiNbO_5$ and $Sn^{2+}/K_4Nb_6O_{17}$ showed the highest activity. However, the photocatalytic activity decreased with the reaction time due to the oxidization of unstable Sn^{2+} by photogenerated holes at the initial stage. The unstable Sn^{2+} species also contributed to the initial high H_2 evolution rate observed at the initial stage. For photocatalytic O_2 production reaction in $AgNO_3$

solution, only $Sn^{2+}/K_4Nb_6O_{17}$ exhibited activity under visible light irradiation due to the more stable Sn^{2+} species existed in the interlayer.

Okamoto et al. recently reported a Rhodium-doped calcium niobate material, $KCa_2Nb_{3-x}Rh_xO_{10-\delta}$, the corresponding proton-exchanged $HCa_2Nb_{3-x}Rh_xO_{10-\delta}$, and exfoliated $Ca_2Nb_{3-x}Rh_xO_{10-\delta}$ nanosheets [100]. $KCa_2Nb_{3-x}Rh_xO_{10-\delta}$ with different Rh dopant was prepared by a simple solid state reaction. **Fig. 17** shows the schematic structure of the Rh-doped nanosheets (building unit of the $KCa_2Nb_{3-x}Rh_xO_{10-\delta}$ compound). It is composed of NbO_6 unit and part of the NbO_6 unit was suggested to be replaced by RhO_6 unit due to the similar ionic radius of Rh^{3+} and Nb^{5+}. However, because the ionic radius of Rh^{3+} is slightly larger than that of Nb^{5+}, the doping of Rh^{3+} leads to a smaller increase of in the unit cell parameters, which corresponds well with the gradual shift of the diffraction peaks to smaller angel upon Rh^{3+} doping. Moreover, Rh was found to be doped into the lattice instead of loaded on the surface of the parent compound. Typical Rh(0.03)-doped $KCa_2Nb_{3-x}Rh_xO_{10-\delta}$, $HCa_2Nb_{3-x}Rh_xO_{10-\delta}$, and corresponding nanosheets aggregate powder showed strong absorption in the visible region as indicated in the UV-Vis spectra and the yellow colour of the samples (**Fig. 18**). Photocatalytic H_2 production reaction was carried out in the presence of aqueous methanol solution under solar irradiation. $KCa_2Nb_{3-x}Rh_xO_{10-\delta}$ was found to show negligible activity for H_2 production while $Ca_2Nb_{3-x}Rh_xO_{10-\delta}$ nanosheets showed drastically enhanced photocatalytic activity. In the $KCa_2Nb_{3-x}Rh_xO_{10-\delta}$ compound, it is supposed that the Rh species present in the bulk have no direct contact with reaction media. On the contrary, most of the Rh species in the Rh-doped nanosheets are very close to the surface because of the extremely small sheet thickness of *ca.* 1 nm. Therefore, the RhO_6 site can work as an efficient electron capture site and result in a

significant improvement in the photocatalytic activity. Even $Ca_2Nb_{3-x}Rh_xO_{10-\delta}$ nanosheets exhibited absorption in the visible region, it didn't show any activity for water splitting under irradiation at wavelength longer than 420 nm.

For LDH materials, Parida et al. reported the incorporation of Fe^{3+} into Mg-Al LDH framework for photocatalytic H_2 generation under visible light irradiation [101]. A series of (Mg/Al + Fe)-CO_3 LDHs with a constant ratio of Mg/(Al + Fe) of 2 : 1 were prepared with a simple co-precipitation method. Upon Fe^{3+} incorporation in the brucite layer, the absorption of the resulting materials was gradually red-shifted toward the visible region with the increase of the Fe^{3+} content. Photocatalytic H_2 production was carried out in aqueous methanol solution under visible light. It was found that there was a correlation between the photocatalytic activities of the LDH materials with the amount of Fe^{3+} dopant. The optimum activity was obtained when the Al/Fe ratio was 4:1, while higher or lower Al/Fe ratio will impair the photocatalytic activity. It was suggested that at proper Al/Fe ratio, the layer framework of the LDH was well crystallized together with abundant surface, hydroxyl groups, and good light absorption properties, and hence high photocatalytic activity was obtained. However, at low Al/Fe ratio, Fe will not substitute Al in the brucite structure but form amorphous Fe_2O_3 which act the recombination centres of the photogenerated charges, while high Al/Fe ratio will lead to poor absorption property of the resulting LDH materials. The doping of metal ions in pristine LDH materials to induce visible light absorption and corresponding photocatalytic activity has been reported in several types of LDH materials [102,103].

2.4 "Dye" sensitization and nanohybrid materials

Non-metal or metal doping into ion-exchangeable materials and the corresponding nanosheets will partially substitute the oxygen atom or cations in the pristine wide band-gap materials, which is supposed to be the origin of the visible light response. Several strategies that can introduce visible light "centre" without substituting the parent atoms have been shown to be effective in imparting visible light absorption and corresponding functionality to the parent materials. In essence, this is a kind of sensitization of the parent samples by the foreign centre due to the strong coupling between the two components and in some cases it can be regarded as a kind of "quasi" doping. Generally, exfoliated nanosheets derived from ion-exchangeable materials have been widely investigated as the building block in this type of "quasi" band-gap engineering.

Liu et al. reported the band-gap narrowing of $Ti_{0.91}O_2$ nanosheets by homogeneous incorporation of molecular iodine (I_2) [104]. **Fig. 19** shows the schematic processes of coupling $Ti_{0.91}O_2$ nanosheets with I_2 molecules. $Ti_{0.91}O_2$ nanosheets were first prepared by an intercalation-exfoliation process. Iodine ethanol solution was then added to the $Ti_{0.91}O_2$ nanosheets aqueous solution to allow the absorption of the nonpolar I_2 molecules on the negatively-charged nanosheets. Finally, I_2-$Ti_{0.91}O_2$ nanosheets were restacked with the addition of aqueous HCl. With this process, most of the I_2 was found to be incorporated into the composite I_2-$Ti_{0.91}O_2$ materials as shown in **Fig. 19**. The amount of I_2 incorporated can be tuned by changing the amount of I_2 used during the synthesis and found to have great influence on the light absorption property of the resulting I_2-$Ti_{0.91}O_2$ nanosheets. When the amount of I_2 is less than 0.4%, only an additional tail-like absorption in the visible region appeared. However, when the amount of I_2 was increased to 1.2%, strong band-to-band absorption with edge of up to

470 nm was observed, corresponding to the drastic decrease of the band-gap from 3.29 to 2.38 eV upon I_2 addition (**Fig. 20**). It is suggested by the authors that the homogeneous molecular I_2 doping within the galleries of the flocculated I_2-$Ti_{0.91}O_2$ sheets cannot realize full long-range coupling at low concentration. Only when the density of I_2 molecules on the surface of the $Ti_{0.91}O_2$ sheets reaches a certain value, strong band-to-band excitation can be achieved. DFT calculations indicated the origin of the visible light absorption at high doping I_2 levels is ascribed to the up-shifting of the valence band maximum (VBM) upon I_2 doping. Moreover, an effective interaction between molecular iodine and $Ti_{0.91}O_2$ nanosheets was indicated from experimental and theoretical analysis.

Different nanoclusters with visible light absorption can also be assembled together with nanosheets to prepare visible-light active composite photocatalyst. Hwang et al. reported the preparation of porous CrO_x-$Ti_{1.83}O_4$ nanohybrid photocatalyst with 1:1 type ordered heterostructure [105]. The nanohybrid is synthesized through hybridization between chromia clusters and exfoliated titanate nanosheets as shown in **Fig. 21**. The nanohybrid was found to have a large surface area and an intense absorption of visible light, ascribed, respectively, to the formation of a porous structure and the hybridization of titanate with narrow band-gap chromium oxide. After calcination of the sample at 673 K, the CrO_x-$Ti_{1.83}O_4$ nanohybrid exhibited an enhanced photocatalytic activity to effectively decompose organic compounds under visible light irradiation ($\lambda > 420$ nm) due to the complete removal of organic residues and better electronic coupling and electrical connectivity between host lattice and guest species. This study highlights the exfoliation–restacking strategy as a very powerful way to develop efficient visible-light-harvesting photocatalysts with excellent thermal stability.

Hwang et al. extended the exfoliation–restacking strategy to prepare CdS quantum dots (QDs) – layered titanate nanosheets hybrid photocatalysts [106]. By dropping colloidal suspension of the exfoliated titanate nanosheets into the aqueous suspension of CdS QDs followed by refluxing, CdS QDs with particle size of ca. 2.5 nm were incorporated in the porous assembly of the titanate nanosheets as shown in **Fig. 22**. Due to the very-limited crystal dimension of two semiconductors, the electronic structure of CdS QDs is strongly coupled with that of the layered titanate nanosheets, leading to an efficient electron transfer between two components and enhanced photo-stability of CdS. The most interesting feature of this nanohybrid lies in its quite high efficiency for the photocatalytic H_2 production from Na_2S-Na_2SO_3 solution under visible light irradiation in the absence of any cocatalyst (such as Pt). On the contrary, only negligible photocatalytic activity was observed on traditional cocatalyst-free CdS-TiO_2 systems. The drastically enhanced photocatalytic activity observed on CdS QDs – titanate nanosheets hybrid was ascribed to the increased lifetime of the electrons and holes, the decrease of the band-gap energy, and the expansion of the surface area upon hybridization. This exfoliation–restacking strategy has also been used for the synthesis of a series of nanohybrid materials composed of different building blocks which delivered unique photocatalytic activity in the visible region [107-116].

Different types of nanosheets were also assembled to obtain nanosheets composite assembly through careful design and control. Gunjakar et al. reported the preparation of mesoporous ordered nanohybrids of 2D Zn-Cr-LDH nanosheets and layered titanium oxide counterparts [117]. The nanohybrids were prepared by layer-by-layer self-assembly between positively charged Zn-Cr-LDH nanosheets and negatively charged layered titanium oxide nanosheets in aqueous solution under constant stirring

(**Fig. 23**). The porosity of the composite can be controllable by changing the ratio of the two components. The obtained hetero-layered nanohybrids showed a strong absorption in the visible region, and an effective electronic coupling between the two component nanosheets was suggested. Under visible light irradiation, the activity of the resultant hetero-layered nanohybrids was *ca.* twice of that obtained on pristine Zn-Cr-LDH material for photocatalytic O_2 production in the presence of $AgNO_3$ sacrificial reagent. Moreover, the chemical stability of the Zn-Cr-LDH nanosheets was improved compared with that of Zn-Cr-LDH due to the protection of the LDH by layered titanate. This study demonstrated the usefulness of the hybridization between cationic and anionic inorganic 2D nanosheets in developing highly efficient visible light active photocatalysts with improved chemical stability. In the following work, Gunjakar et al. prepared an electrostatically derived self-assembly of Zn–Cr-LDH 2D nanoplates with graphene 2D nanosheets with a highly porous stacked structure [118]. The positively charged Zn–Cr-LDH nanoplates were found to be immobilized on the surface of negatively charged graphene nanosheets in the as-prepared nanohybrids. The Zn–Cr-LDH–RGO nanohybrid shows much higher photocatalytic activity for visible light induced O_2 generation than the Zn–Cr-LDH–GO nanohybrid due to the hybridization with RGO. This finding demonstrated the superior advantage of graphene nanosheets as the platform for improving the photocatalytic activity of 2D nanostructured inorganic solids.

The origin of visible light absorption for the above mentioned samples are from inorganic semiconductors materials. Several classical dye-sensitized systems using organic dye sensitizer in combination with ion-exchangeable materials or nanosheets have been developed in recent years. Hong et al. constructed a dye-sensitized system

using LDH materials for photocatalytic H_2 generation under visible light [119]. The system is composed of well-dispersed layered Mg-Al LDH as the support to immobilize inexpensive photosensitizer (rose bengal, RB) and photocatalyst (Pt). Under visible light irradiation, the photosensitizer absorbed light and injected excited electrons to the Pt catalysts supported on the LDH substrate (**Fig. 24**). Protons will then be reduced to produce H_2 and the photosensitizer will be quenched by the triethanolamine (TEOA) electron donor. The photocatalytic activity of this self-assembled RB–LDH–Pt system is a few times more than that from the free system (without LDH). Four advantages were suggested for this RB–LDH–Pt system compared with those without LDH support, such as suppressed self-quenching of dye due to the immobilization, formation of well-dispersed catalyst nanoparticles on the support, efficient charge transfer between dye molecules and catalyst nanoparticles due to the close arrangement, and high recyclability of the expensive catalyst.

Mallouk et al. reported a dye-sensitized system composed of calcium niobate nanosheets, $HCa_2Nb_3O_{10}$, which immobilize Ruthenium sensitizer and Pt catalyst for photocatalytic H_2 generation [120]. Unilamellar colloidal $Ca_2Nb_3O_{10}$ nanosheets were prepared with well-developed intercalation-exfoliation process followed by restacking of the $Ca_2Nb_3O_{10}$ nanosheets to obtain $HCa_2Nb_3O_{10}$. The $HCa_2Nb_3O_{10}$-Ru dye-Pt system showed activity for photocatalytic H_2 production from aqueous EDTA solutions under visible light ($\lambda = 450 \pm 20$ nm). Contrary to $HCa_2Nb_3O_{10}$-Pt system, the performance of $HCa_2Nb_3O_{10}$-Ru dye-Pt was not significantly affected by the structural properties of $HCa_2Nb_3O_{10}$ while primarily governed by the electron injection efficiency from the excited-state sensitizer into the $HCa_2Nb_3O_{10}$ nanosheets. Therefore, improving

the charge-transfer from the dye to the support is crucial for this kind of dye-sensitized system.

2.5 Investigation with different characterization techniques and theoretical calculations

The fact that the absorption of wide band-gap semiconductor materials can be extended to the visible light region after appropriate treatment arouses the interest on the origin why visible light absorption can be induced. Different characterisation techniques can help to clarify this point. UV-Vis diffuse reflectance spectroscopy gives direct information on the absorption properties of ion-exchangeable materials before and after modification. X-ray photoelectron spectroscopy helps to identify the chemical state for the elements in the materials especial those for the functional dopants that play the role of introducing visible light absorption. X-ray diffraction analysis in combination with transmission electron microscopy, scanning electron microscopy, atomic force microscopy, and X-ray absorption Fine Structure analysis can identify the structural properties of the ion-exchangeable materials. In particular, atomic force microscopy is very powerful in investigating nanosheets-based systems which are derived from bulk ion-exchangeable materials. Although these characterization techniques have been widely used to investigate ion-exchangeable materials with visible light absorption feature, theoretical calculation especially density functional theory calculation has demonstrated to be quite powerful in investigating semiconductor materials from fundamental understanding aspects. In fact, theoretical calculations have been successfully used to study many groups of visible light-responsive semiconductor materials, including ion-exchangeable semiconductor materials [6,67,79,85,86,102,104].

As shown in **Fig. 8**, $Cs_{0.68}Ti_{1.83}O_{4-x}N_x$ and $H_{0.68}Ti_{1.83}O_{4-x}N_x$ show strong band-to-band visible light absorption instead of weak tail-like absorption commonly observed on N-doped TiO_2. The visible light absorption for both materials is ascribed to the doping of N in the original crystal lattice. However, for N-doped TiO_2, only some localized states are formed in the intrinsic band-gap of TiO_2 due to the small amount of N dopant and consequently small visible light absorption shoulder is induced by inhomogeneous nitrogen doping near the particle surface. On the contrary, DFT calculations indicate that the valence bands of $Cs_{0.68}Ti_{1.83}O_{4-x}N_x$ and $H_{0.68}Ti_{1.83}O_{4-x}N_x$ are mainly spanned by O_{2p} and mixed with N_{2p} orbitals and the N $_{2p}$ orbitals contribute to the formation of the top of the valence band, which leads to the upward shift of VBM (**Fig. 25**). Moreover, due to the high amount of N dopant and its homogeneous distribution in $Cs_{0.68}Ti_{1.83}O_4$ and $H_{0.68}Ti_{1.83}O_4$, strong band-to-band absorption and significantly narrowed bands are achieved [79]. DFT calculations also indicated that $H_{0.68}Ti_{1.83}O_{4-x}N_x$ has much deeper conduction band minimum than $Cs_{0.68}Ti_{1.83}O_{4-x}N_x$, which is in good agreement with the experimental result and partially explains why different photocatalytic activities are achieved on the two materials. Similar phenomena regarding theoretical calculations were observed on N-doped $CsTaWO_6$ and $HTaWO_6$ semiconductor materials [85,86].

Zhao et al. investigated a family of visible light-responsive photocatalysts obtained by doping CrO_6 octahedra into a LDH matrix [102]. By using DFT calculation, it was found that the VBM and CBM of the resulting CuCr-LDH are located at the same Z point, indicating the CuCr-LDH is a direct semiconductor. This transition nature is anticipated lead to facile separation of photogenerated electron-hole pairs upon light irradiation. The densities of states (DOS) and partial densities of states (PDOS) of

CuCr-NO_3-LDH indicate that the VBM is primarily composed of occupied Cr 3d orbitals, while the CBM is mainly dominated by unoccupied Cr 3d orbitals. Moreover, the CBM is composed of two parts with slightly different band energies and result in different optical transitions, which is in good agreement with the two strong visible light absorption band of CuCr-NO_3-LDH. Therefore, the visible light response of the CuCr-NO_3-LDH materials originates from the d-d transition in the dispersed CrO_6 octahedron in the LDH layer, which partially contributes to the strong photocatalytic activity of a series of Cr-containing LDHs.

For the "dye" sensitized $Ti_{0.91}O_2$–iodine sample, theoretical calculations also give reasonable insight in lieu of experimental results [104]. From the calculations, it is found that iodine atoms prefer to form iodine molecules. Moreover, due to the $Ti_{0.91}O_2$–iodine and iodine-iodine atomic and molecular interactions, iodine atoms tend to form stable clusters, rather than simply assembling as isolated iodine molecules or atoms. The calculated DOS profiles suggest that the iodine's contribution to the formation of the electronic states in the band-gap of $Ti_{0.91}O_2$ can be divided qualitatively into two parts (**Fig. 26**). One is very close to the VBM and the other one is near the middle of the band-gap, and both parts are highly dependent on the amount of iodine adsorbed on $Ti_{0.91}O_2$. At low level of iodine, both parts in the DOS profile are highly localized and can only form isolated states. However, at higher level of iodine, the delocalized states overlap with VBM, therefore contributing to an elevated VBM and a widened valence band. More importantly, homogeneous distribution of sufficient I_2 within the $Ti_{0.91}O_2$ nanosheets can exert accumulative interactions strong enough to drastically modify the electronic band structures of the $Ti_{0.91}O_2$–iodine sample. This explains well about the UV-Vis absorption characteristic of two $Ti_{0.91}O_2$–iodine samples

shown in **Fig. 20**. Therefore, theoretical calculations can not only add deeper understanding to the electronic structure-related the light absorption and photocatalytic activity but may provide valuable guidance for the future development of highly efficient visible light-responsive photocatalysts.

3. Photocatalytic applications of visible light-responsive ion-exchangeable materials

Up to now, visible light-responsive ion-exchangeable materials have been widely applied to different photocatalytic applications, such as solar H_2 production from photocatalytic and photoelectrochemical water splitting, pollutant degradation for environmental remediation, and chemical synthesis. Table 1 gives a summary on the recent results achieved on using ion-exchangeable layered materials for visible light-induced photocatalysis, especially some representative samples. One typical sample is $H_{0.68}Ti_{1.83}O_{4-x}N_x$ catalyst. This material is characteristic of the strong band-to-band visible light absorption, high surface area, high oxidation powder of photogenerated holes, and therefore this material shows much higher photocatalytic activity for the degradation of organic pollutants than N-doped titania photocatalysts in the visible region [79]. Moreover, the delaminated N-$Ti_{0.91}O_{2-x}N_x$ nanosheets can be used as the building block for the fabrication of nanosheets-based devices, which showed drastically enhanced photoelectrochemical performance for water splitting than the undoped one [81]. For LDH materials, it was reported that (Zn/Cr) LDH showed visible light absorption and achieved quantum efficiency of 60.9% for water oxidation in the presence of $AgNO_3$ as the sacrificial reagents under visible light irradiation (λ >420 nm) [73]. This reported value is among one of the highest value for water oxidation under visible light irradiation, indicating the great potential of using this kind

of material for solar H_2 production from photoelectrochemical water splitting or photocatalytic water splitting in Z-scheme system. It was also reported that in some nanosheet-based hybrid system, due to the strong coupling between the parent nanosheet and the foreign clusters, efficient photocatalytic H_2 production can be produced without loading any expensive cocatalyst, which is highly desirable for the practical applications [106]. Therefore, ion-exchangeable materials have been an important family of semiconductor materials that have potential applications for solar fuel production and environmental remediation.

4. Conclusions and outlook

Advances on the recent development of visible light-responsive ion-exchangeable semiconductor material for solar H_2 generation or environmental remediation were summarized in this paper. Several attractive features associated with the unique crystal structures and the resulting appreciable light absorption and photocatalytic properties were demonstrated on these materials. For examples, ion-exchangeable layered materials can provide spatially-separated photocatalytic oxidation and reduction reaction sites, which are believed to retard the recombination of photogenerated electron-holes and lead to high photocatalytic performance. The unique layered or open structure of the ion-exchangeable materials can facilitate the homogeneous doping of foreign elements, especially anions, in the lattice of the pristine materials, which can drastically modify the electronic structure of the pristine materials and lead to drastically enhanced photocatalytic performance in the visible region. Moreover, ion-exchangeable materials can be exfoliated into ultrathin 2D nanosheets using proper wet-chemical approaches, and these nanosheets can act as versatile building blocks for the fabrication of efficient composite photocatalytic materials and devices. Therefore,

ion-exchangeable materials represent one unique type of semiconductor materials which showed potential applications in the field of solar energy conversion. However, it should be noted that several problems such as the decreased oxidation power and stability may exist due to the elevation of the valence band level, and introduction of defects/recombination centres during band-gap engineering process.

Regarding ion-exchangeable materials, research work from the following aspects should be considered in the future. First, the development of ion-exchangeable semiconductor-based materials or systems capable of splitting pure water under visible light is highly desirable. Up to now, there is still no report on using ion-exchangeable materials for overall water splitting under visible light even many cases have been reported for overall water splitting under UV light. As one of the "Holy Grail" of chemistry, this work represents significant challenges while at the same time tremendous opportunity. The overall water splitting could be achieved by choosing the proper ion-exchangeable materials in combination with suitable band engineering strategies. For example, the simultaneous doping of anion-anion (for instance F-N co-doping), cation-cation (both in the layer lattice and inter-galleries) may compensate the charge imbalance due to the mono-doping and stabilize the crystal structures of the pristine materials, which will lead to efficient photocatalytic performance. Moreover, by combining ion-exchangeable materials with appropriate candidates in a Z-scheme system, overall water splitting under visible light is anticipated to be realized. To our understanding, one of most possible ways to split water is to use ion-exchangeable materials-based photoelectrochemical devices with external bias, which has not attracted much attention up to now. Second, the development of efficient visible light-responsive ion-exchangeable materials with wider light absorption range is highly

desirable. For example, Service pointed out that the energy conversion efficiency must be ≥ 10% if the economic feasibility of the PEC hydrogen generation can be met [121]. This requires that the band-gap of the semiconductor materials must be less than 2.4 eV even the solar energy conversion efficiency of 100% is assumed during the calculation. As semiconductor materials with smaller band-gap can absorb more solar energy and have higher theoretical solar energy conversion efficiency, the development of ion-exchangeable materials with excellent light absorption properties will be more desirable toward practical applications. Last but importantly, the fundamental understanding of phototcatalytic reactions that proceed on ion-exchangeable materials is crucial for advancing the development of highly efficient photocatalysts. For example, the photocatalytic reaction mechanism associated with the unique crystal structure of ion-exchangeable materials needs to be further investigated. Theoretical calculations in combination with different time-resolved characterization techniques (infrared, fluoresce, etc.) will help to provide insight into these nanoscale surface phenomenon.

Acknowledgements

This project was supported by Australian Research Council (through its DP programs) and Queensland State Government Smart State program (NIRAP).

References

[1] R. M. Navarro, M. C. Alvarez-Galvan, J. A. V. de la Mano, S. M. Al-Zahrani, J. L. G. Fierro, Energy Environ. Sci. 3 (2010) 1865.
[2] A. L. Linsebigler, G. Q. Lu, J. T. Yates, Chem. Rev. 95 (1995) 735.
[3] A. J. Bard, M. A. Fox, Acc. Chem. Res. 28 (1995) 141.
[4] A. Fujishima, K. Honda, Nature 238 (1972) 37.
[5] A. Fujishima, X. T. Zhang, D. A. Tryk, Surf. Sci. Rep. 63 (2008) 515.
[6] A. Kudo, Y. Miseki, Chem. Soc. Rev. 38 (2009) 253.
[7] M. Osada, T. Sasaki, J. Mater. Chem. 19 (2009) 2503.
[8] R. Z. Ma, T. Sasaki, Adv. Mater. 22 (2010) 5082.
[9] M. Osada, T. Sasaki, Adv. Mater. 24 (2012) 210.

[10] L. Z. Wang, Y. Ebina, K. Takada, K. Kurashima, T. Sasaki, Adv. Mater. 16 (2004) 1412.
[11] L. Z. Wang, K. Takada, A. Kajiyama, M. Onoda, Y. Michiue, L. Q. Zhang, M. Watanabe, T. Sasaki, Chem. Mater. 15 (2003) 4508.
[12] L. Z. Wang, Y. Omomo, N. Sakai, K. Fukuda, I. Nakai, Y. Ebina, K. Takada, M. Watanabe, T. Sasaki, Chem. Mater. 15 (2003) 2873.
[13] L. Wang, T. Sasaki, Y. Ebina, K. Kurashima, M. Watanabe, Chem. Mater. 14 (2002) 4827.
[14] L. Z. Wang, Y. Ebina, K. Takada, T. Sasaki, Chem. Commun. (2004) 1074.
[15] B. Seger, J. McCray, A. Mukherji, X. Zong, Z. Xing, L. Wang, Angew. Chem. Int. Ed. (2013) DOI: 10.1002/anie.201302062.
[16] A. Kudo, T. Kondo, J. Mater. Chem. 7 (1997) 777.
[17] Y. Inoue, T. Kubokawa, K. Sato, J. Phys. Chem. 95 (1991) 4059.
[18] T. Takata, Y. Furumi, K. Shinohara, A. Tanaka, M. Hara, J. N. Kondo, K. Domen, Chem. Mater. 9 (1997) 1063.
[19] S. Ikeda, M. Hara, J. N. Kondo, K. Domen, H. Takahashi, T. Okubo, M. Kakihana, Chem. Mater. 10 (1998) 72.
[20] M. Shibata, A. Kudo, A. Tanaka, K. Domen, K. Maruya, T. Onishi, Chem. Lett. (1987) 1017.
[21] K. Domen, A. Kudo, M. Shibata, A. Tanaka, K. Maruya, T. Onishi, J. Chem. Soc., Chem. Commun. (1986) 1706.
[22] A. Kudo, A. Tanaka, K. Domen, K. Maruya, K. Aika, T. Onishi, J. Catal. 111 (1988) 67.
[23] A. Kudo, K. Sayama, A. Tanaka, K. Asakura, K. Domen, K. Maruya, T. Onishi, J. Catal. 120 (1989) 337.
[24] K. Sayama, A. Tanaka, K. Domen, K. Maruya, T. Onishi, J. Catal. 124 (1990) 541.
[25] K. Domen, J. N. Kondo, M. Hara, T. Takata, Bull. Chem. Soc. Jpn. 73 (2000) 1307.
[26] K. Domen, J. Yoshimura, T. Sekine, A. Tanaka, T. Onishi, Catal. Lett. 4 (1990) 339.
[27] M. Machida, K. Miyazaki, S. Matsushima, M. Arai, J. Mater. Chem. 13 (2003) 1433.
[28] M. Machida, J.-i. Yabunaka, T. Kijima, Chem. Mater. 12 (2000) 812.
[29] A. Kudo, H. Okutomi, H. Kato, Chem. Lett. 29 (2000) 1212.
[30] T. Mitsuyama, A. Tsutsumi, T. Hata, K. Ikeue, M. Machida, Bull. Chem. Soc. Jpn. 81 (2008) 401.
[31] Y. Matsumoto, S. Ida, T. Inoue, J. Phys. Chem. C 112 (2008) 11614.
[32] H. Kato, K. Asakura, A. Kudo, J. Am. Chem. Soc. 125 (2003) 3082.
[33] Z. B. Chen, T. F. Jaramillo, T. G. Deutsch, A. Kleiman-Shwarsctein, A. J. Forman, N. Gaillard, R. Garland, K. Takanabe, C. Heske, M. Sunkara, E. W. McFarland, K. Domen, E. L. Miller, J. A. Turner, H. N. Dinh, J. Mater. Res. 25 (2010) 3.
[34] Z. G. Yi, J. H. Ye, N. Kikugawa, T. Kako, S. X. Ouyang, H. Stuart-Williams, H. Yang, J. Y. Cao, W. J. Luo, Z. S. Li, Y. Liu, R. L. Withers, Nat. Mater. 9 (2010) 559.
[35] A. Kudo, K. Omori, H. Kato, J. Am. Chem. Soc. 121 (1999) 11459.
[36] I. Tsuji, H. Kato, A. Kudo, Angew. Chem. Int. Ed. 44 (2005) 3565.
[37] I. Tsuji, H. Kato, H. Kobayashi, A. Kudo, J. Am. Chem. Soc. 126 (2004) 13406.
[38] K. Maeda, K. Teramura, K. Domen, J. Catal. 254 (2008) 198.
[39] X. Wang, K. Maeda, A. Thomas, K. Takanabe, G. Xin, J. M. Carlsson, K. Domen, M. Antonietti, Nat. Mater. 8 (2009) 76.
[40] G. Hitoki, T. Takata, J. N. Kondo, M. Hara, H. Kobayashi, K. Domen, Chem. Commun. (2002) 1698.
[41] A. Ishikawa, T. Takata, J. N. Kondo, M. Hara, H. Kobayashi, K. Domen, J. Am. Chem. Soc. 124 (2002) 13547.
[42] A. Ishikawa, Y. Yamada, T. Takata, J. N. Kondo, M. Hara, H. Kobayashi, K. Domen, Chem. Mater. 15 (2003) 4442.

[43] X. Zong, H. J. Yan, G. P. Wu, G. J. Ma, F. Y. Wen, L. Wang, C. Li, J. Am. Chem. Soc. 130 (2008) 7176.
[44] R. Asahi, T. Morikawa, T. Ohwaki, K. Aoki, Y. Taga, Science 293 (2001) 269.
[45] X. Zong, Z. Xing, H. Yu, Z. G. Chen, F. Q. Tang, J. Zou, G. Q. Lu, L. Z. Wang, Chem. Commun. (2011) 11742.
[46] S. U. M. Khan, M. Al-Shahry, W. B. Ingler, Science 297 (2002) 2243.
[47] M. Kitano, K. Funatsu, M. Matsuoka, M. Ueshima, M. Anpo, J. Phys. Chem. B 110 (2006) 25266.
[48] H. Irie, Y. Watanabe, K. Hashimoto, J. Phys. Chem. B 107 (2003) 5483.
[49] H. Irie, Y. Watanabe, K. Hashimoto, Chem. Lett. 32 (2003) 772.
[50] T. Umebayashi, T. Yamaki, H. Itoh, K. Asai, Appl. Phys. Lett. 81 (2002) 454.
[51] T. Umebayashi, T. Yamaki, S. Tanaka, K. Asai, Chem. Lett. 32 (2003) 330.
[52] A. Hattori, H. Tada, J. Sol-Gel Sci. Technol. 22 (2001) 47.
[53] A. Hattori, K. Shimoda, H. Tada, S. Ito, Langmuir 15 (1999) 5422.
[54] W. Zhao, W. H. Ma, C. C. Chen, J. C. Zhao, Z. G. Shuai, J. Am. Chem. Soc. 126 (2004) 4782.
[55] X. Hong, Z. Wang, W. Cai, F. Lu, J. Zhang, Y. Yang, N. Ma, Y. Liu, Chem. Mater. 17 (2005) 1548.
[56] J. C. Yu, L. Z. Zhang, Z. Zheng, J. C. Zhao, Chem. Mater. 15 (2003) 2280.
[57] H. Meier, Photochem. Photobiol. 16 (1972) 219.
[58] S. Anderson, E. C. Constable, M. P. Dareedwards, J. B. Goodenough, A. Hamnett, K. R. Seddon, R. D. Wright, Nature 280 (1979) 571.
[59] E. Borgarello, J. Kiwi, E. Pelizzetti, M. Visca, M. Graetzel, J. Am. Chem. Soc 103 (1981) 6324.
[60] J. Moser, M. Graetzel, J. Am. Chem. Soc 106 (1984) 6557.
[61] R. Abe, J. Photochem. Photobiol. C-Photochem. Rev. 11 (2010) 179.
[62] M. D. Hernandez-Alonso, F. Fresno, S. Suarez, J. M. Coronado, Energy Environ. Sci. 2 (2009) 1231.
[63] Y. Inoue, Energy Environ. Sci. 2 (2009) 364.
[64] R. M. Navarro, M. C. Sanchez-Sanchez, M. C. Alvarez-Galvan, F. del Valle, J. L. G. Fierro, Energy Environ. Sci. 2 (2009) 35.
[65] M. G. Walter, E. L. Warren, J. R. McKone, S. W. Boettcher, Q. X. Mi, E. A. Santori, N. S. Lewis, Chem. Rev. 110 (2010) 6446.
[66] H. Tong, S. X. Ouyang, Y. P. Bi, N. Umezawa, M. Oshikiri, J. H. Ye, Adv. Mater. 24 (2012) 229.
[67] X. B. Chen, S. H. Shen, L. J. Guo, S. S. Mao, Chem. Rev. 110 (2010) 6503.
[68] A. Kudo, Int. J. Hydrogen Energy 31 (2006) 197.
[69] G. Liu, L. Z. Wang, H. G. Yang, H. M. Cheng, G. Q. Lu, J. Mater. Chem. 20 (2010) 831.
[70] J. Yoshimura, Y. Ebina, J. Kondo, K. Domen, A. Tanaka, J. Phys. Chem. 97 (1993) 1970.
[71] I. Tsuji, A. Kudo, J. Photochem. Photobiol., A 156 (2003) 249.
[72] H. G. Kim, D. W. Hwang, J. S. Lee, J. Am. Chem. Soc. 126 (2004) 8912.
[73] C. G. Silva, Y. Bouizi, V. Fornes, H. Garcia, J. Am. Chem. Soc. 131 (2009) 13833.
[74] Y. Lee, J. H. Choi, H. J. Jeon, K. M. Choi, J. W. Lee, J. K. Kang, Energy Environ. Sci. 4 (2011) 914.
[75] K. Parida, L. Mohapatra, Dalton Trans. 41 (2012) 1173.
[76] K. M. Parida, L. Mohapatra, Chem. Eng. J. 179 (2012) 131.
[77] L. Tian, Y. F. Zhao, S. He, M. Wei, X. Duan, Chem. Eng. J. 184 (2012) 261.
[78] N. Baliarsingh, L. Mohapatra, K. Parida, J. Mater. Chem. A 1 (2013) 4236.
[79] G. Liu, L. Z. Wang, C. H. Sun, X. X. Yan, X. W. Wang, Z. G. Chen, S. C. Smith, H. M. Cheng, G. Q. Lu, Chem. Mater. 21 (2009) 1266.

[80] G. Liu, P. Niu, L. Z. Wang, G. Q. Lu, H. M. Cheng, Catal. Sci. Technol. 1 (2011) 222.
[81] G. Liu, L. Z. Wang, C. H. Sun, Z. G. Chen, X. X. Yan, L. Cheng, H. M. Cheng, G. Q. Lu, Chem. Commun. (2009) 1383.
[82] Y. Wang, C. H. Sun, X. X. Yan, F. X. Xiu, L. Z. Wang, S. C. Smith, K. L. Wang, G. Q. Lu, J. Zou, J. Am. Chem. Soc. 133 (2011) 695.
[83] M. Guo, G. Q. Lu, X. F. Zhu, C. X. Wu, L. Z. Wang, Colloids and Surfaces A: Physicochem. Eng. Aspects 395 (2012) 100.
[84] M. Guo, C. F. Su, G. Q. Lu, X. F. Zhu, C. X. Wu, L. Z. Wang, Thin Solid Films 520 (2012) 7066.
[85] A. Mukherji, R. Marschall, A. Tanksale, C. H. Sun, S. C. Smith, G. Q. Lu, L. Z. Wang, Adv. Func. Mater. 21 (2011) 126.
[86] C. H. Sun, A. Mukherji, G. Liu, L. Z. Wang, S. C. Smith, Chem. Phys. Lett. 501 (2011) 427.
[87] R. Marschall, A. Mukherji, A. Tanksale, C. H. Sun, S. C. Smith, L. Z. Wang, G. Q. Lu, J. Mater. Chem. 21 (2011) 8871.
[88] X. K. Li, N. Kikugawa, J. H. Ye, Adv. Mater. 20 (2008) 3816.
[89] X. K. Li, N. Kikugawa, J. H. Ye, Chem. Eur. J. 15 (2009) 3538.
[90] X. Zong, C. H. Sun, Z. G. Chen, A. Mukherji, H. Wu, J. Zou, S. C. Smith, G. Q. Lu, L. Z. Wang, Chem. Commun. 47 (2011) 6293.
[91] Z. Zhai, Y. C. Huang, L. Xu, X. Y. Yang, C. H. Hu, L. H. Zhang, Y. N. Fan, W. H. Hou, Nano Res. 4 (2011) 635.
[92] Y. F. Huang, Y. L. Wei, S. H. Cheng, L. Q. Fan, Y. B. Li, J. M. Lin, J. H. Wu, Sol. Energy Mater. Sol. Cells 94 (2010) 761.
[93] X. K. Li, B. Yue, J. H. Ye, Appl. Catal. A-Gen. 390 (2010) 195.
[94] X. K. Li, H. Q. Pan, Q. S. Hu, C. Zhang, J. Alloys Compd. 509 (2011) 6252.
[95] Z. Zhai, C. H. Hu, X. Y. Yang, L. H. Zhang, C. Liu, Y. N. Fan, W. H. Hou, J. Mater. Chem. 22 (2012) 19122.
[96] S. Ida, Y. Okamoto, M. Matsuka, H. Hagiwara, T. Ishihara, J. Am. Chem. Soc 134 (2012) 15773.
[97] Y. Matsumoto, M. Koinuma, Y. Iwanaga, T. Sato, S. Ida, J. Am. Chem. Soc 131 (2009) 6644.
[98] Y. Hosogi, H. Kato, A. Kudo, J. Phys. Chem. C 112 (2008) 17678.
[99] Y. Hosogi, Y. Shimodaira, H. Kato, H. Kobayashi, A. Kudo, Chem. Mater. 20 (2008) 1299.
[100] Y. Okamoto, S. Ida, J. Hyodo, H. Hagiwara, T. Ishihara, J. Am. Chem. Soc 133 (2011) 18034.
[101] K. Parida, M. Satpathy, L. Mohapatra, J. Mater. Chem. 22 (2012) 7350.
[102] Y. F. Zhao, S. T. Zhang, B. Li, H. Yan, S. He, L. Tian, W. Y. Shi, J. Ma, M. Wei, D. G. Evans, X. Duan, Chem. Eur. J. 17 (2011) 13175.
[103] K. Parida, L. Mohapatra, N. Baliarsingh, J. Phys. Chem. C 116 (2012) 22417.
[104] G. Liu, C. H. Sun, L. Z. Wang, S. C. Smith, G. Q. Lu, H. M. Cheng, J. Mater. Chem. 21 (2011) 14672.
[105] T. W. Kim, S. G. Hur, S. J. Hwang, H. Park, W. Choi, J. H. Choy, Adv. Func. Mater. 17 (2007) 307.
[106] H. N. Kim, T. W. Kim, I. Y. Kim, S. J. Hwang, Adv. Func. Mater. 21 (2011) 3111.
[107] X. X. Yan, G. Liu, L. Z. Wang, Y. Wang, X. F. Zhu, J. Zou, G. Q. Lu, J. Mater. Res. 25 (2010) 182.
[108] T. W. Kim, S. J. Hwang, S. H. Jhung, J. S. Chang, H. Park, W. Choi, J. H. Choy, Adv. Mater. 20 (2008) 539.
[109] B. Z. Lin, L. W. He, B. L. Zhu, Y. L. Chen, B. F. Gao, Catal. Commun. 29 (2012) 166.
[110] J. Fu, Y. L. Tian, B. B. Chang, G. N. Li, F. N. Xi, X. P. Dong, J. Solid State Chem. 196 (2012) 282.

[111] Z. Zhai, X. Y. Yang, L. Xu, C. H. Hu, L. H. Zhang, W. H. Hou, Y. N. Fan, Nanoscale 4 (2012) 547.
[112] T. W. Kim, H. W. Ha, M. J. Paek, S. H. Hyun, I. H. Baek, J. H. Choy, S. J. Hwang, J. Phys. Chem. C 112 (2008) 14853.
[113] H. Liu, B. Z. Lin, L. W. He, H. Qu, P. Sun, B. F. Gao, Y. L. Chen, Chem. Eng. J. 215 (2013) 396.
[114] B. Z. Lin, B. H. Xu, L. W. He, X. R. Fan, H. Qu, Microporous Mesoporous Mat. 172 (2013) 105.
[115] H. Hattori, Y. Ide, S. Ogo, K. Inumaru, M. Sadakane, T. Sano, ACS Catal. 2 (2012) 1910.
[116] Y. Ide, M. Matsuoka, M. Ogawa, J. Am. Chem. Soc. 132 (2010) 16762.
[117] J. L. Gunjakar, T. W. Kim, H. N. Kim, I. Y. Kim, S. J. Hwang, J. Am. Chem. Soc 133 (2012) 14998.
[118] J. L. Gunjakar, I. Y. Kim, J. M. Lee, N. S. Lee, S. J. Hwang, Energy Environ. Sci. 6 (2013) 1008.
[119] J. D. Hong, Y. B. Wang, J. S. Pan, Z. Y. Zhong, R. Xu, Nanoscale 3 (2011) 4655.
[120] K. Maeda, M. Eguchi, W. J. Youngblood, T. E. Mallouk, Chem. Mater. 21 (2009) 3611.
[121] R. F. Service, Science 297 (2002) 2189.

Table 1. Summary of visible light-responsive ion-exchangeable materials for various photocatalytic applications

Type	Semiconductor materials	Band-gap (eV)	Application	Reaction conditions	Reference
Pristine materials					

	$RbPb_2Nb_3O_{10}$ and $HPb_2Nb_3O_{10}$	2.5	photocatalytic H_2 (15 μmol h^{-1}) or O_2 (1.1 μmol h^{-1}) production	500 W Xe lamp (λ>420 nm), aqueous methanol solution (H_2 production) or $AgNO_3$ solution (O_2 production)	[70]
	Zn/Ti, Zn/Ce, Zn/Cr LDHs	—	photocatalytic O_2 production, (apparent quantum yield of 60.9% at 410 nm)	200 W Xenon-doped mercury lamp (λ>400 nm), aqueous $AgNO_3$ solution	[73]
	Ni/Ti and Cu/Ti LDHs	—	photocatalytic O_2 production (49 and 31μmol in 6 h)	300 W xenon lamp (400 nm < λ< 700 nm), aqueous $AgNO_3$ solution	[74]
	carbonate-intercalated Zn/Cr LDH	—	photocatalytic H_2 production (1732 μmol in 3 h)	125 W Hg lamp (λ>400 nm), aqueous methanol solution	[75]
	Zn/Fe LDH	2.2-2.4	pollutant degradation (more than 90% degradation rate in 2 h)	Nature sun light, aqueous methyl violet or malachite green solution	[76]
	Cu/Cr LDH film	—	pollutant degradation	300 W xenon lamp (λ>400 nm), 2,4,6-trichlorophenol (2,4,6-TCP), sulforhodamine B (SRB) and Congo red solution	[77]
	Ni-Zn/Cr LDH	—	photocatalytic H_2 production (1915 μmol)	125 W Hg lamp (λ>400 nm), aqueous methanol solution	[78]
non-metal doped materials					
	N-doped $Cs_{0.68}Ti_{1.83}O_4$ and $H_{0.68}Ti_{1.83}O_4$	2.7-2.9	pollutant degradation (Activity is higher than that of benchmark N-doped P25.)	300 W Xe lamp (λ>420 nm), aqueous Rhodamine G solution.	[79,80]
	N-doped $Ti_{0.91}O_2$ nanosheets	—	Photoelectrochemical water splitting (< 10 μA at 0.7 V *vs.* Ag/AgCl)	300 W Xe lamp (λ>420 nm), 0.1 M NaOH solution	[81]
	N-doped or N and S co-doped $CsTaWO_6$ and $HTaWO_6$	2.4	photocatalytic H_2 production (147 μmol h^{-1})	300 W Xe lamp with AM1.5 filter, aqueous ethanol solution	[85-87]
	N-doped HNb_3O_8	2.7	pollutant degradation, (Activity is higher than that of benchmark	300 W Xe lamp (λ>420 nm), Rhodamine B solution	[88]

			N-doped P25.)		
	N-doped $H_2Ti_4O_9$	2.8	pollutant degradation (total degradation in 1 h) and photocatalytic H_2 production (6 μmol h^{-1})	300 W Xe lamp (λ>420 nm), Rhodamine B solution or aqueous methanol solution	[89, 93]
	N-doped $CsCa_2Ta_3O_{10}$	2.1	photocatalytic O_2 production (72 μmol h^{-1} g^{-1})	300 W Xe lamp (λ>400 nm), aqueous $AgNO_3$ solution	[90]
	N-doped $CsCa_2Ta_3O_{10}$ nanosheet	2.1	photocatalytic H_2 and O_2 production (showed < 1μmol h^{-1} for pure water splitting)	500 or 300 W Xe lamp, aqueous methanol solution (H_2 production), $AgNO_3$ solution (O_2 production) or pure water	[96]
	N-doped $HTiNbO_5$ and $HTiNbO_5$ nanosheet	—	pollutant degradation (Activity is higher than that of benchmark N-doped P25.)	300 W Xe lamp (λ>420 nm), Rhodamine B solution	[91]
	N-doped $K_4Nb_6O_{17}$,$KCa_2Nb_3O_{10}$, $K_2Ti_4O_9$, and $KTiNbO_5$	—	Photocatalytic H_2 production (1.2 μmol h^{-1})	500 W Xe lamp (λ>420 nm), water	[97]
metal doped materials					
	Sn^{2+}-doped $KTiNbO_5$, $K_4Nb_6O_{17}$, $CsTi_2NbO_7$, $K_2Ti_4O_9$, $K_2Ti_2O_5$, and $Cs_2Ti_6O_{13}$	2.5-2.8	photocatalytic H_2 (54 μmol h^{-1})and O_2 (4 μmol h^{-1}) production with depredated activity	300 W Xe lamp (λ>420 nm), aqueous methanol solution (H_2 production) or $AgNO_3$ solution (O_2 production)	[98]
	Rh-doped $KCa_2Nb_{3-x}Rh_xO_{10-\delta}$, $HCa_2Nb_{3-x}Rh_xO_{10-\delta}$, and $Ca_2Nb_{3-x}Rh_xO_{10-\delta}$ nanosheets	—	photocatalytic H_2 production (quantum efficiency of 65% at 300 nm) and photoelectrochemical water splitting (300 uA at 1 V *vs.* Ag/AgCl)	500 W Xe lamp, aqueous methanol solution (H_2 production) or Na_2SO_4 solution.	[100]
	Fe-doped Mg/Al LDH	1.9-2.8	photocatalytic H_2 production (301 μmol h^{-1} g^{-1})	125 W Hg lamp (λ>400 nm), aqueous methanol solution	[101]
	Cr-doped Zn,Co, or Ni-based LDH	—	pollutant degradation (more than 80% degradation rate	Sulforhodamine-B (SRB) and Congo Red	[102]

			in 6 h)		
	Co-doped Cu/Cr LDH	1.7-2.5	pollutant degradation (more than 80% degradation rate in 4 h)	Nature sun light, MB solution	[103]
sensitization and nanohybrid					
	I_2-$Ti_{0.91}O_2$ nanohybrid	2.4	pollutant degradation(more than 80% degradation rate in 1 h)	300 W Xe lamp (λ>420 nm), Rhodamine B solution	[104]
	CrO_x–$Ti_{1.83}O_4$ nanohybrid	—	pollutant degradation (54 μmol of phenol was degraded)	400 W Xe arc lamp (λ>420 nm), acid orange 7 and phenol solution	[105]
	CdS quantum dots–titanate nanosheets hybrid	2.9	photocatalytic H_2 production (1 mmol h^{-1} g^{-1})	300 W Xe lamp (λ>420 nm), Na_2S-Na_2SO_3 aqueous solution	[106]
	Zn/Cr LDH nanosheet–titanate nanosheets hybrid	2.8	photocatalytic O_2 production (1.18 mmol h^{-1} g^{-1})	450 W Xe arc lamp (λ>420 nm), aqueous $AgNO_3$ solution	[117]
	Zn/Cr LDH nanosheet–graphene nanosheet hybrid	2.8	photocatalytic O_2 production (1.2 mmol h^{-1} g^{-1})	450 W Xe arc lamp (λ>420 nm), aqueous $AgNO_3$ solution	[118]
	Rose Bengal–sensitized Mg/Al LDH	—	photocatalytic H_2 production (Turnover number of 304)	300 W Xe lamp (λ>420 nm), aqueous Triethanolamine (TEOA) solution	[119]
	RuP^{2+}–sensitized $HCa_2Nb_3O_{10}$	—	photocatalytic H_2 production (7.1 μmol h^{-1})	300 W Xe lamp (λ > 450 ± 20 nm), ethylenediaminetetraacetic acid (EDTA) solution	[120]
	SiO_2-pillared N-doped $H_2Ti_4O_9$	2.9	pollutant degradation (Activity is higher than that of benchmark N-doped P25.) and photocatalytic H_2 production (6 μmol h^{-1})	300 W xenon arc lamp (λ>420 nm), aqueous Rhodamine B solution or methanol solution	[93,94]
	Mn-$TaWO_6$ nanosheets hybrid	2.5	pollutant degradation (more than 90% degradation rate in 3 h)	300 W xenon arc lamp (λ>420 nm), aqueous methylene blue solution	[109]
	Mn-titanate nanosheets hybrid	2.6	pollutant degradation (Activity is higher than that of	300 W xenon arc lamp (λ>420 nm), aqueous methylene blue solution	[110]

		benchmark N-doped P25.)		
Co-$TaWO_6$ nanosheets hybrid	2.4	pollutant degradation (90% degradation rate in 2 h)	300 W Xe lamp (λ>420 nm), aqueous methylene blue solution	[113]
NiO-$HTiNbO_5$ nanosheet hybrid	—	pollutant degradation (more than 90% degradation rate in 100 min)	300 W Xe lamp (λ>420 nm), aqueous Rhodamine B solution	[111]
FeO_x-titanate nanosheets hybrid	2.3	pollutant degradation with improved stability	400 W Xe arc lamp (λ>420 nm) aqueous methylene blue solution	[112]
Co-titanate nanosheets hybrid	2.2	pollutant degradation (more than 90% degradation rate in 3 h)	300 W xenon arc lamp (λ>420 nm), aqueous methylene blue solution	[114]
FeO_x-titanate nanosheets hybrid	2.3	chemical synthesis(0.33% yield and 99% selectivity)	Solar simulator (1000 W m^{-2}) cyclohexane acetonitrile solution	[115]
Au-titanate nanosheets hybrid	—	chemical synthesis (62% yield and 96% selectivity)	150 W Xe lamp (λ>420 nm), aqueous benzene	[116]

Figure Captions

Fig. 1. Schematic steps for photocatalytic reactions that occur on semiconductor surface.

Fig. 2. Schematic crystal structures of ion-exchangeable (a) lepidocrocite-type $Cs_{0.68}Ti_{1.83}O_4$ oxide, and (b) Layered Double Hydroxide (LDH). Reprinted with permission from Ref.[73, 79]. Copyright 2009 American Chemical Society.

Fig. 3. Model of the movements of the photoproduced electron and hole at the TiO_x nanosheet with a lepidocrosite-type structure. The electron moves in the 3d CB consisting of the Ti^{4+} network in the nanosheet and then reduces Ag^+ and Cu^{2+} at the edge, while the hole exists at the 2p VB consisting of the O^{2-} surface and oxidizes Mn^{2+}

on the surface. Reprinted with permission from Ref.[31]. Copyright 2008 American Chemical Society.

Fig. 4. Strategies of developing visible light-responsive photocatalysts for water splitting. (A) Find materials with suitable valence band (VB) or conduction band (CB) levels. (B) Formation of doping level in the forbidden band through foreign elements doping, and (C) Sensitization of wide band-gap materials with small band-gap materials or organic dye in a composite material.

Fig. 5. Schematic crystal structure of $RbPb_2Nb_3O_{10}$. Reprinted with permission from Ref.[70]. Copyright 1993 American Chemical Society.

Fig. 6. Schematic mechanisms of H_2 evolution over $Pt/HPb_2Nb_3O_{10}$. (a) Pt exists only on the external surface from H_2PtCl_6 source. (b) Pt exists in the interlayer from $[Pt(NH_3)_4]Cl_2$ source. Reprinted with permission from Ref.[70]. Copyright 1993 American Chemical Society.

Fig. 7. Diffuse reflectance UV-Vis spectra (plotted as the Kubelka-Munk function of the reflectance, *R*) of (a) (Zn/Ti)LDH, (b) (Zn/Ce)LDH, and (c) (Zn/Cr)LDH. Inset: Diffuse reflectance UV-vis spectra of (Zn/Cr)LDH (A) before and (B) after calcination at 723 K. Reprinted with permission from Ref.[73]. Copyright 2009 American Chemical Society.

Fig. 8. UV-visible light absorption spectra of (a) $Cs_{0.68}Ti_{1.83}O_4$, (b) $Cs_{0.68}Ti_{1.83}O_{4-x}N_x$, (c) $H_{0.68}Ti_{1.83}O_4$, (d) $H_{0.68}Ti_{1.83}O_{4-x}N_x$, (e) commercial P25 titania, and (f) N-doped P25 prepared by calcining P25 powders in ammonia atmosphere at 823 K for 1 h. The inset is the photos of samples of (a) $Cs_{0.68}Ti_{1.83}O_4$, (b) $Cs_{0.68}Ti_{1.83}O_{4-x}N_x$, (c) $H_{0.68}Ti_{1.83}O_4$, (d) $H_{0.68}Ti_{1.83}O_{4-x}N_x$. Reprinted with permission from Ref.[79]. Copyright 2009 American Chemical Society.

Fig. 9. Schematic of procedures for preparing nitrogen-doped $Ti_{0.91}O_2$ nanosheets. TBA^+: tetrabutylammonium ion. Reprinted with permission from Ref.[81]. Copyright 2009 Royal Society of Chemistry.

Fig. 10. (a) Tapping-mode AFM image of the first (PEI–$Ti_{0.91}O_{2-x}N_x$) bilayer deposited on a silicon wafer. (b) UV-visible light absorbance spectra of the colloidal suspension of $Ti_{0.91}O_2$ (A) and $Ti_{0.91}O_{2-x}N_x$ (B) nanosheets. The insert gives the photographs of colloidal suspensions of $Ti_{0.91}O_2$ (white) and $Ti_{0.91}O_{2-x}N_x$ (yellow) nanosheets. Reprinted with permission from Ref.[81]. Copyright 2009 Royal Society of Chemistry.

Fig. 11. Schematic structure of N-doped $CsTaWO_6$. Atoms N, O, $Ta_{0.5}W_{0.5}$, and Cs are illustrated as black, red, blue, and yellow spheres, respectively. Reprinted with permission from Ref.[85]. Copyright 2011 WILEY-VCH Verlag GmbH & Co. KGaA, Weinheim.

Fig. 12. UV-Visible diffuse reflectance spectra of the nitrogen-doped as well as the undoped HNb_3O_8 and Nb_2O_5 samples. The insets show the pictures of the HNb_3O_8 and N-HNb_3O_8 samples. Reprinted with permission from Ref.[88]. Copyright 2008 WILEY-VCH Verlag GmbH & Co. KGaA, Weinheim.

Fig. 13. Schematic structure of N-doped $CsCa_2Ta_3O_{10}$. N, O, TaO_6 unit, Ca, and Cs are illustrated as deep blue, red, light blue, green, and purple spheres, respectively. Reprinted with permission from Ref.[90]. Copyright 2011 Royal Society of Chemistry.

Fig. 14. Time courses of hydrogen evolution over $Ca_2Ta_3O_{9.7}N_{0.2}$ nanosheets, the protonated form of the nanosheets H-$Ca_2Ta_3O_{9.7}N_{0.2}$ and the parent layered oxynitride ($CsCa_2Ta_3O_{9.7}N_{0.2}$) under (a) full arc irradiation and (b) visible light irradiation (> 400

nm). The amount of catalyst: 10 mg, co-catalyst: 0.15 wt.% Rh-loaded samples. Reprinted with permission from Ref.[96]. Copyright 2011 American Chemical Society.

Fig. 15. Proposed mechanism for the N doping in nanosheet during UV irradiation. Reprinted with permission from Ref.[97]. Copyright 2009 American Chemical Society.

Fig. 16. Schematic illustration of (a) the origin of visible light absorption of layered metal oxides ion-exchanged with Sn^{2+} and (b) band structure of layered metal oxides ion-exchanged with Sn^{2+}. Reprinted with permission from Ref.[98]. Copyright 2008 American Chemical Society.

Fig. 17. Crystal structure of Rh-doped calcium niobate nanosheet prepared by exfoliation of layered and photocatalytic reaction model in water/methanol system. Reprinted with permission from Ref.[100]. Copyright 2011 American Chemical Society.

Fig. 18. UV-vis spectra and photograph of the Rh(0.03)-doped samples. (a); Rh(0.03)-doped parent layered $KCa_2Nb_{3-x}Rh_xO_{10-\delta}$ powder, (b); Rh(0.03)-doped $HCa_2Nb_{3-x}Rh_xO_{10-\delta}$ powder, (c); Rh(0.03)-doped Ca-Nb-O nanosheets aggregate powders, and (d); non-doped Ca-Nb-O nanosheets aggregate powder. Reprinted with permission from Ref.[100]. Copyright 2011 American Chemical Society.

Fig. 19. Schematic of the formation processes of coupling $Ti_{0.91}O_2$ nanosheets with I_2 molecules. The bottom panel gives corresponding products at different stages of preparing (1.2%) I_2-$Ti_{0.91}O_2$ sheets: (A), suspension of $Ti_{0.91}O_2$ nanosheets; (B), iodine ethanol solution; (C), suspension of $Ti_{0.91}O_2$ nanosheets coupled with I_2 molecules; (D), flocculated $Ti_{0.91}O_2$ nanosheets coupled with I_2 molecules. Reprinted with permission from Ref.[104]. Copyright 2011 Royal Society of Chemistry.

Fig. 20. Plots of transformed Kubelka-Munk function versus the energy of light recorded from the flocculated (X%) I_2-$Ti_{0.91}O_2$ nanosheet sheets with different amounts of I_2 molecules doped: a, X=0; b, X=0.4; c, X= 1.2. Reprinted with permission from Ref.[104]. Copyright 2011 Royal Society of Chemistry.

Fig. 21. Schematic diagram for an exfoliation–hybridization route to the preparation of CrO_x-$Ti_{1.83}O_4$ nanohybrid. Reprinted with permission from Ref.[105]. Copyright 2007 WILEY-VCH Verlag GmbH & Co. KGaA, Weinheim.

Fig. 22. Structural model of CdS QDs – layered titanate nanosheet hybrid. Reprinted with permission from Ref.[106]. Copyright 2011 WILEY-VCH Verlag GmbH & Co. KGaA, Weinheim.

Fig. 23. Schematic process of preparing Zn-Cr-LDH and layered titanium oxide nanosheets assembly, structure of the nanosheet assembly, and photocatalytic activity for O_2 generation. Reprinted with permission from Ref.[117]. Copyright 2011 American Chemical Society.

Fig. 24. Schematic diagram of photocatalytic H_2 generation on RB–LDH–Pt system. Reprinted with permission from Ref.[119]. Copyright 2011 Royal Society of Chemistry.

Fig. 25. (A) Structure model of cesium and protonated titanate. purple colour, Cs or H; red, oxygen; gray, titanium; blue, N. (B) Total DOSs (black line) of $Cs_{0.68}Ti_{1.83}O_4$ ((a)undoped; (b) nitrogen-doped) and $H_{0.68}Ti_{1.83}O_4$ ((c)undoped; (d) nitrogen-doped) and the projected DOSs of O (red line) and doped N (blue line). The dopant N is located at a substitutional site for four O atoms in the employed models for $Cs_{0.68}Ti_{1.83}O_4$ and $H_{0.68}Ti_{1.83}O_4$crystals. Reprinted with permission from Ref.[79]. Copyright 2009 American Chemical Society.

Fig. 26. Structures from DFT optimizations, with oxygen and iodine being indicated as red, white and purple spheres, titanium located at the centres of a gray TiO_6 octahedtron. (a) Adsorption of four iodine atoms on the $Ti_{0.91}O_2$ sheets; (b) Adsorption of eight iodine atoms on the $Ti_{0.91}O_2$ sheets. Calculated density of states for (c) (4 × 4) supercell of pristine $Ti_{0.91}O_2$ sheets; (d) $Ti_{0.91}O_2$ sheets with the adsorption of four iodine atoms; (e) $Ti_{0.91}O_2$ sheets with the adsorption of eight iodine atoms. Reprinted with permission from Ref.[104]. Copyright 2011 Royal Society of Chemistry.

Abbreviations:

LDH: Layered Double Hydroxide

2D: two-dimensional

VBM: valence band maximum

DFT: Density functional theory

DOS: densities of states

PDOS: Partial densities of states

QDs: quantum dots

TBAOH: tetrabutylammonium hydroxide

TEOA: triethanolamine

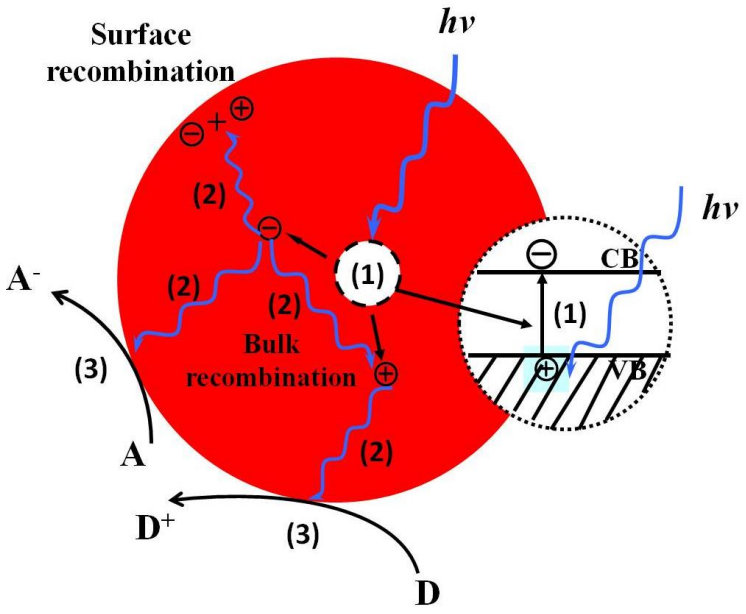

Fig. 1. Schematic steps for photocatalytic reactions that occur on semiconductor surface.

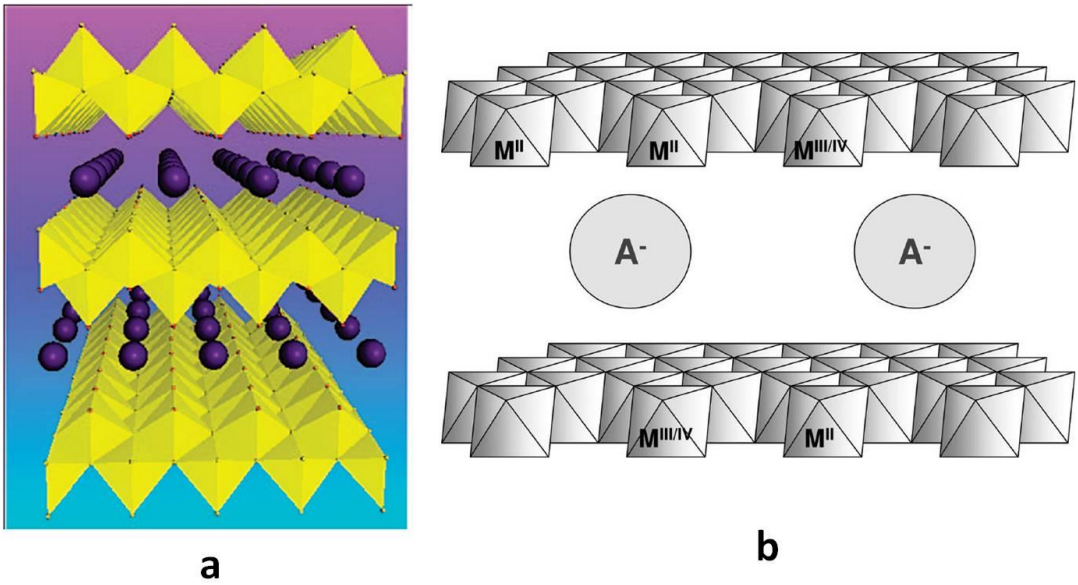

Fig. 2. Schematic crystal structures of ion-exchangeable (a) lepidocrocite-type $Cs_{0.68}Ti_{1.83}O_4$ oxide, and (b) Layered Double Hydroxide (LDH). Reprinted with permission from Ref.[73, 79]. Copyright 2009 American Chemical Society.

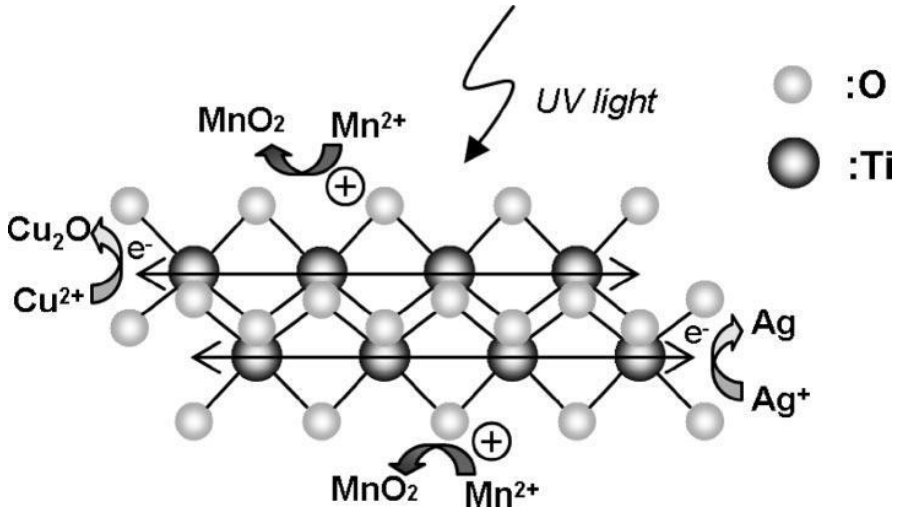

Fig. 3. Model of the movements of the photoproduced electron and hole at the TiO_x nanosheet with a lepidocrosite-type structure. The electron moves in the 3d CB consisting of the Ti^{4+} network in the nanosheet and then reduces Ag^+ and Cu^{2+} at the edge, while the hole exists at the 2p VB consisting of the O^{2-} surface and oxidizes Mn^{2+} on the surface. Reprinted with permission from Ref.[31]. Copyright 2008 American Chemical Society.

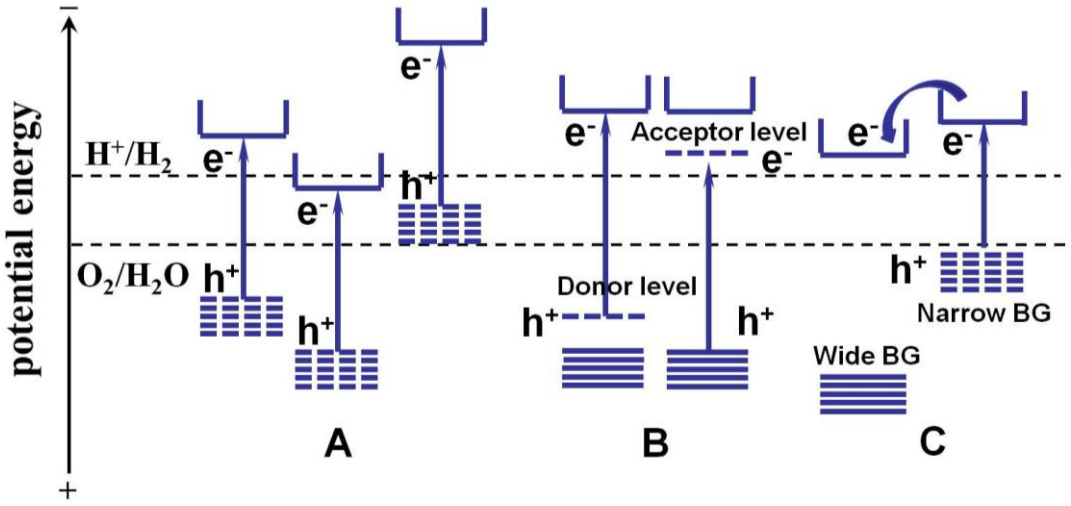

Fig. 4. Strategies of developing visible light-responsive photocatalysts for water splitting. (A) Find materials with suitable valence band (VB) or conduction band (CB) levels. (B) Formation of doping level in the forbidden band through foreign elements doping, and (C) Sensitization of wide band-gap materials with small band-gap materials or organic dye in a composite material.

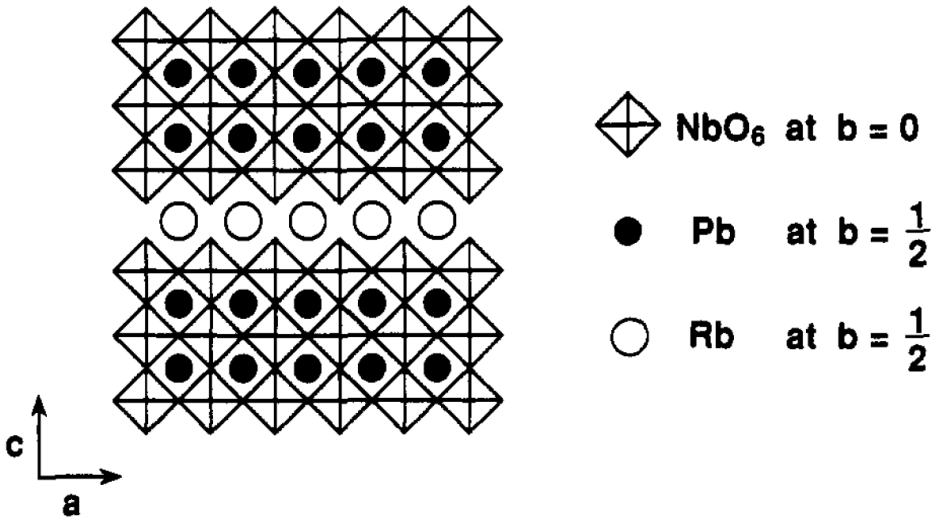

Fig. 5. Schematic crystal structure of $RbPb_2Nb_3O_{10}$. Reprinted with permission from Ref.[70]. Copyright 1993 American Chemical Society.

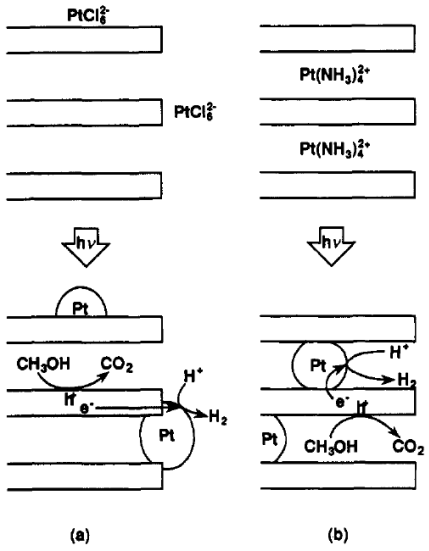

Fig. 6. Schematic mechanisms of H_2 evolution over $Pt/HPb_2Nb_3O_{10}$. (a) Pt exists only on the external surface from H_2PtCl_6 source. (b) Pt exists in the interlayer from $[Pt(NH_3)_4]Cl_2$ source. Reprinted with permission from Ref.[70]. Copyright 1993 American Chemical Society.

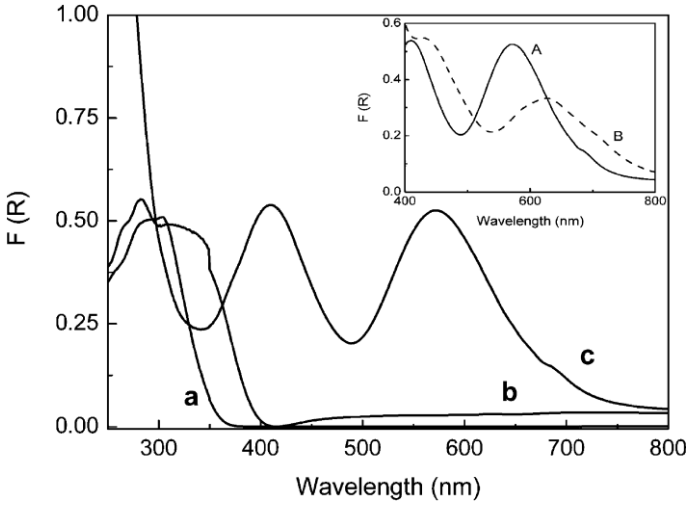

Fig. 7. Diffuse reflectance UV-vis spectra (plotted as the Kubelka-Munk function of the reflectance, *R*) of (a) (Zn/Ti)LDH, (b) (Zn/Ce)LDH, and (c) (Zn/Cr)LDH. Inset: Diffuse reflectance UV-vis spectra of (Zn/Cr)LDH (A) before and (B) after calcination at 723 K. Reprinted with permission from Ref.[73]. Copyright 2009 American Chemical Society.

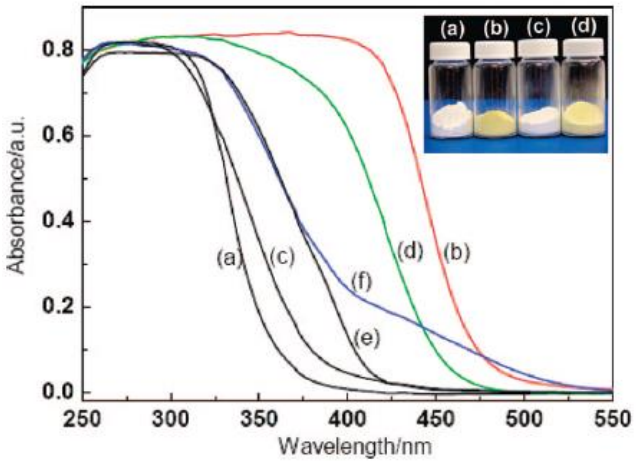

Fig. 8. UV-visible light absorption spectra of (a) $Cs_{0.68}Ti_{1.83}O_4$, (b) $Cs_{0.68}Ti_{1.83}O_{4-x}N_x$, (c) $H_{0.68}Ti_{1.83}O_4$, (d) $H_{0.68}Ti_{1.83}O_{4-x}N_x$, (e) commercial P25 titania, and (f) N-doped P25 prepared by calcining P25 powders in ammonia atmosphere at 823 K for 1 h. The inset is the photos of samples of (a) $Cs_{0.68}Ti_{1.83}O_4$, (b) $Cs_{0.68}Ti_{1.83}O_{4-x}N_x$, (c) $H_{0.68}Ti_{1.83}O_4$, (d) $H_{0.68}Ti_{1.83}O_{4-x}N_x$. Reprinted with permission from Ref.[79]. Copyright 2009 American Chemical Society.

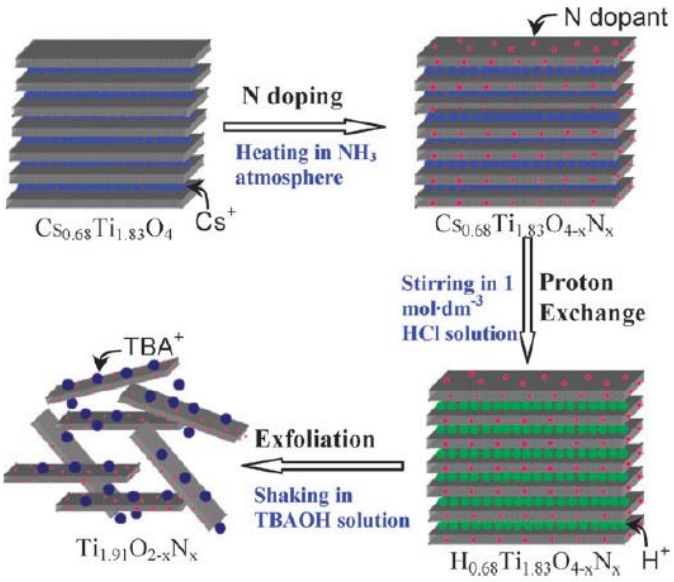

Fig. 9. Schematic of procedures for preparing nitrogen-doped $Ti_{0.91}O_2$ nanosheets. TBA^+: tetrabutylammonium ion. Reprinted with permission from Ref.[81]. Copyright 2009 Royal Society of Chemistry.

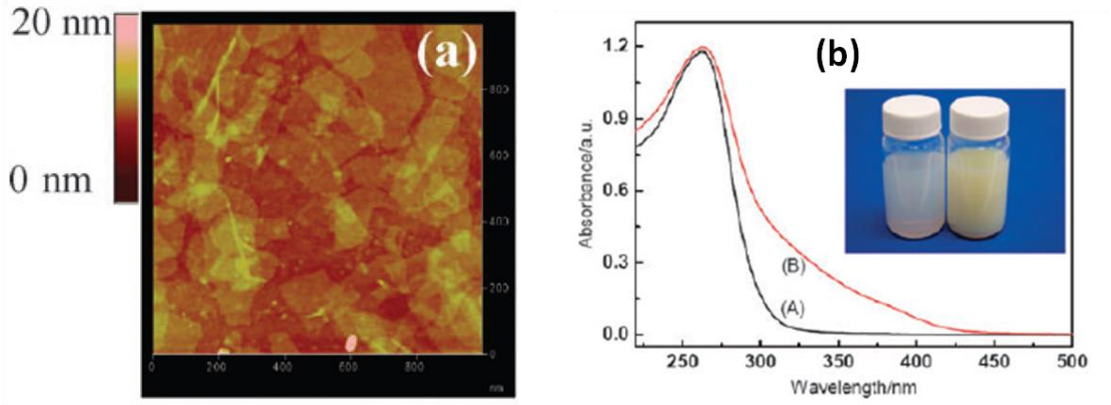

Fig. 10. (a) Tapping-mode AFM image of the first (PEI – $Ti_{0.91}O_{2-x}N_x$) bilayer deposited on a silicon wafer. (b) UV-visible light absorbance spectra of the colloidal suspension of $Ti_{0.91}O_2$ (A) and $Ti_{0.91}O_{2-x}N_x$ (B) nanosheets. The insert gives the photographs of colloidal suspensions of $Ti_{0.91}O_2$ (white) and $Ti_{0.91}O_{2-x}N_x$ (yellow) nanosheets. Reprinted with permission from Ref.[81]. Copyright 2009 Royal Society of Chemistry.

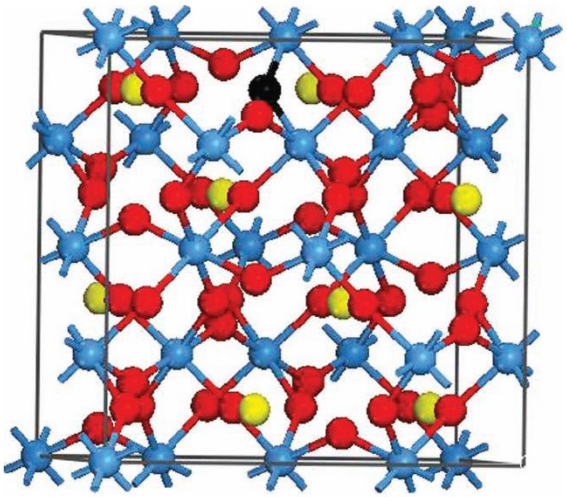

Fig. 11. Schematic structure of N-doped $CsTaWO_6$. Atoms N, O, $Ta_{0.5}W_{0.5}$, and Cs are illustrated as black, red, blue, and yellow spheres, respectively. Reprinted with permission from Ref.[85]. Copyright 2011 WILEY-VCH Verlag GmbH & Co. KGaA, Weinheim.

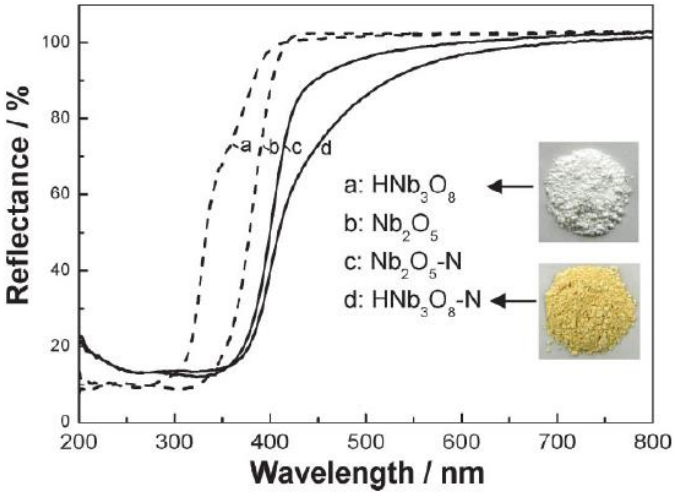

Fig. 12. UV-Visible diffuse reflectance spectra of the nitrogen-doped as well as the undoped HNb_3O_8 and Nb_2O_5 samples. The insets show the pictures of the HNb_3O_8 and N-HNb_3O_8 samples. Reprinted with permission from Ref.[88]. Copyright 2008 WILEY-VCH Verlag GmbH & Co. KGaA, Weinheim.

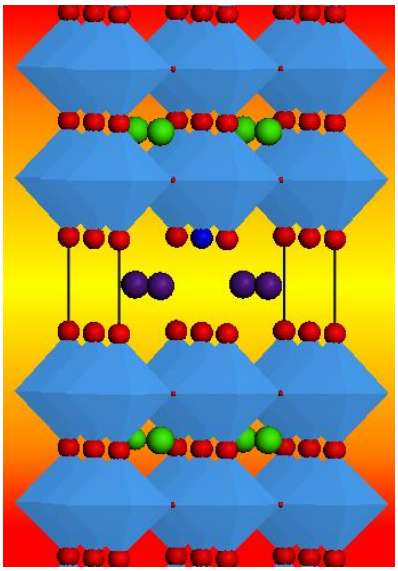

Fig. 13. Schematic structure of N-doped $CsCa_2Ta_3O_{10}$. N, O, TaO_6 unit, Ca, and Cs are illustrated as deep blue, red, light blue, green, and purple spheres, respectively. Reprinted with permission from Ref.[90]. Copyright 2011 Royal Society of Chemistry.

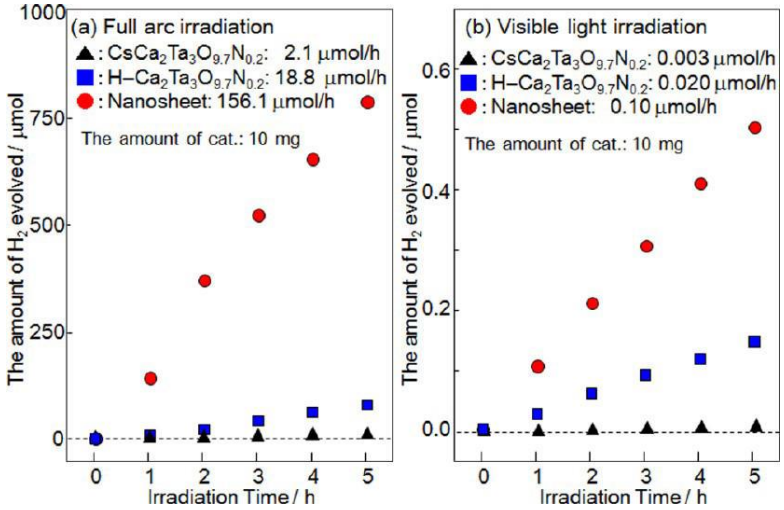

Fig. 14. Time courses of hydrogen evolution over $Ca_2Ta_3O_{9.7}N_{0.2}$ nanosheets, the protonated form of the nanosheets H-$Ca_2Ta_3O_{9.7}N_{0.2}$ and the parent layered oxynitride ($CsCa_2Ta_3O_{9.7}N_{0.2}$) under (a) full arc irradiation and (b) visible light irradiation (> 400 nm). The amount of catalyst: 10 mg, co-catalyst: 0.15 wt.% Rh-loaded samples. Reprinted with permission from Ref.[96]. Copyright 2011 American Chemical Society.

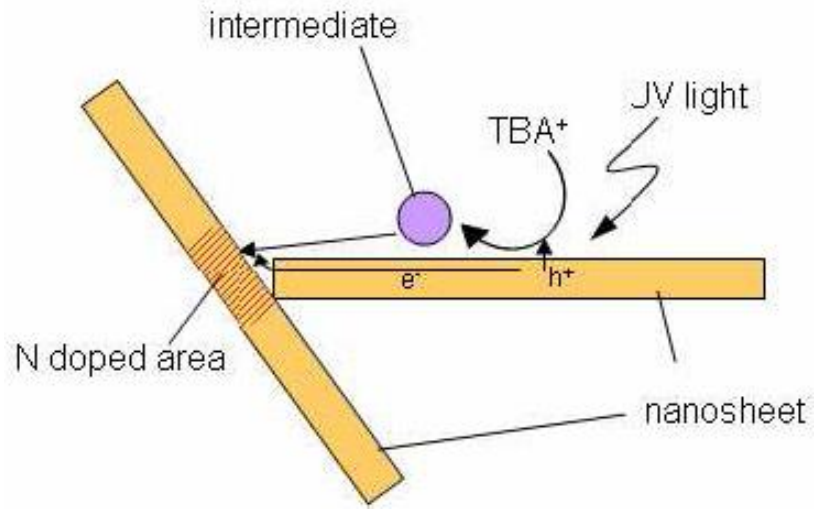

Fig. 15. Proposed mechanism for the N doping in nanosheet during UV irradiation. Reprinted with permission from Ref.[97]. Copyright 2009 American Chemical Society.

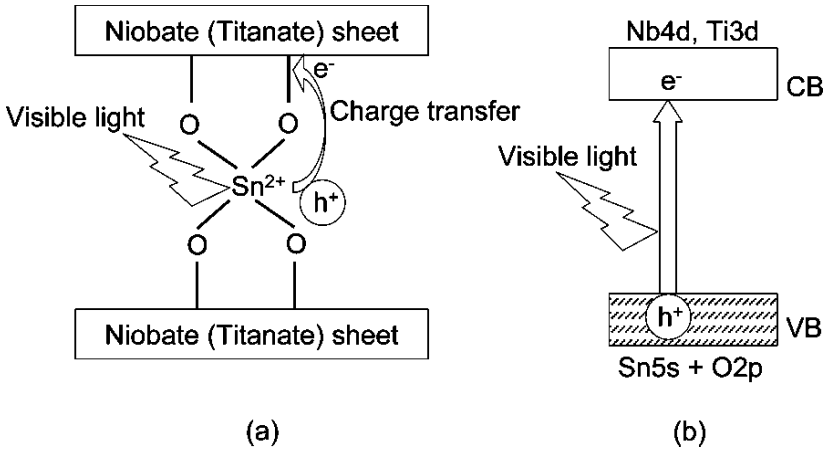

Fig. 16. Schematic illustration of (a) the origin of visible light absorption of layered metal oxides ion-exchanged with Sn^{2+} and (b) band structure of layered metal oxides ion-exchanged with Sn^{2+}. Reprinted with permission from Ref.[98]. Copyright 2008 American Chemical Society.

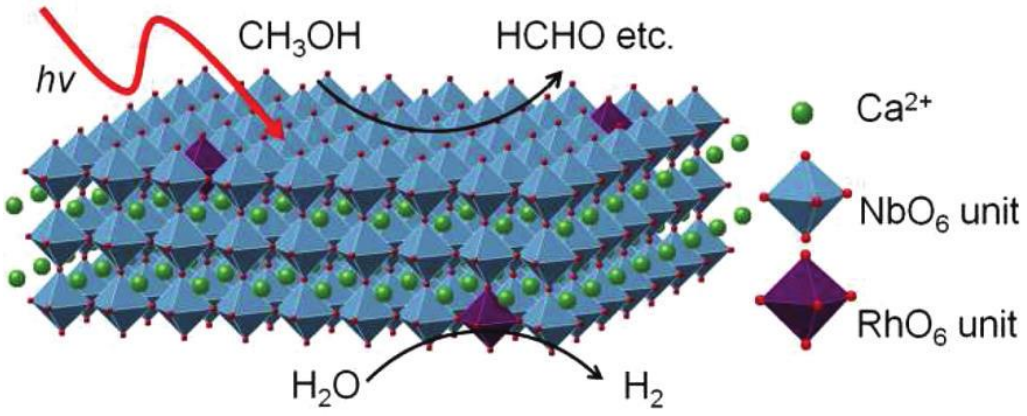

Fig. 17. Crystal structure of Rh-doped calcium niobate nanosheet prepared by exfoliation of layered and photocatalytic reaction model in water/methanol system. Reprinted with permission from Ref.[100]. Copyright 2011 American Chemical Society.

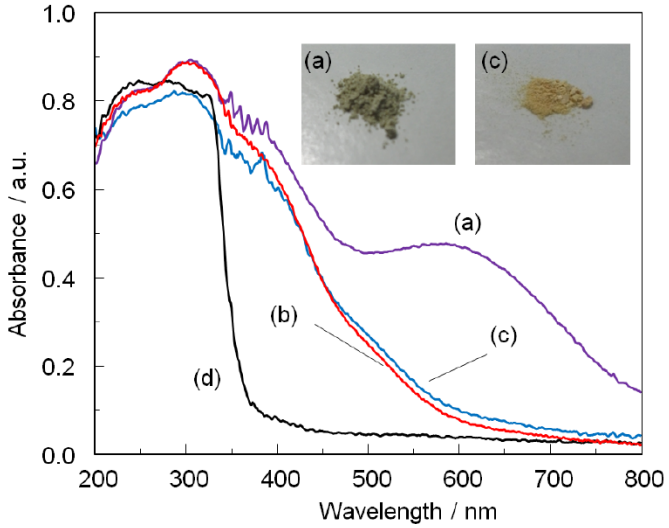

Fig. 18. UV-vis spectra and photograph of the Rh(0.03)-doped samples. (a); Rh(0.03)-doped parent layered $KCa_2Nb_{3-x}Rh_xO_{10-\delta}$ powder, (b); Rh(0.03)-doped $HCa_2Nb_{3-x}Rh_xO_{10-\delta}$ powder, (c); Rh(0.03)-doped Ca-Nb-O nanosheets aggregate powders, and (d); non-doped Ca-Nb-O nanosheets aggregate powder. Reprinted with permission from Ref.[100]. Copyright 2011 American Chemical Society.

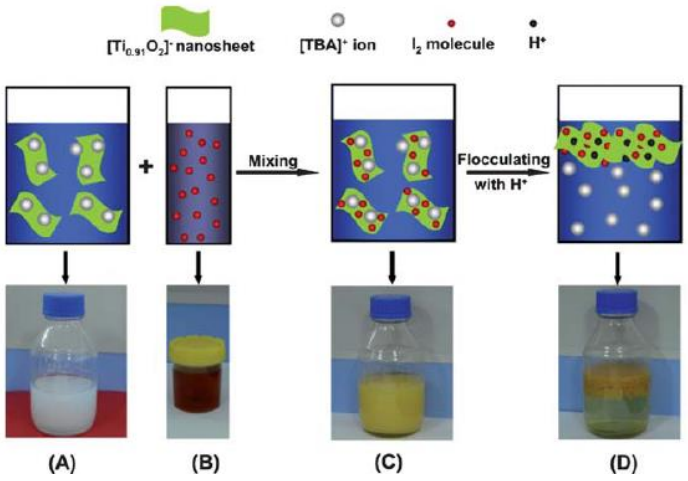

Fig. 19. Schematic of the formation processes of coupling $Ti_{0.91}O_2$ nanosheets with I_2 molecules. The bottom panel gives corresponding products at different stages of preparing (1.2%) I_2-$Ti_{0.91}O_2$ sheets: (A), suspension of $Ti_{0.91}O_2$ nanosheets; (B), iodine ethanol solution; (C), suspension of $Ti_{0.91}O_2$ nanosheets coupled with I_2 molecules; (D), flocculated $Ti_{0.91}O_2$ nanosheets coupled with I_2 molecules. Reprinted with permission from Ref.[104]. Copyright 2011 Royal Society of Chemistry.

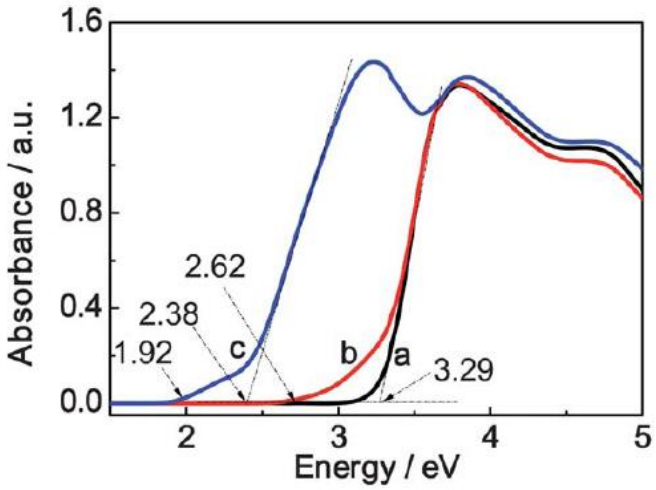

Fig. 20. Plots of transformed Kubelka-Munk function versus the energy of light recorded from the flocculated (X%) I_2-$Ti_{0.91}O_2$ nanosheet sheets with different amounts of I_2 molecules doped: a, X=0; b, X=0.4; c, X= 1.2. Reprinted with permission from Ref.[104]. Copyright 2011 Royal Society of Chemistry.

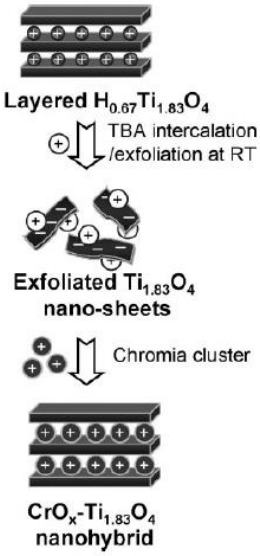

Fig. 21. Schematic diagram for an exfoliation – hybridization route to the preparation of CrO_x-$Ti_{1.83}O_4$ nanohybrid. Reprinted with permission from Ref.[105]. Copyright 2007 WILEY-VCH Verlag GmbH & Co. KGaA, Weinheim.

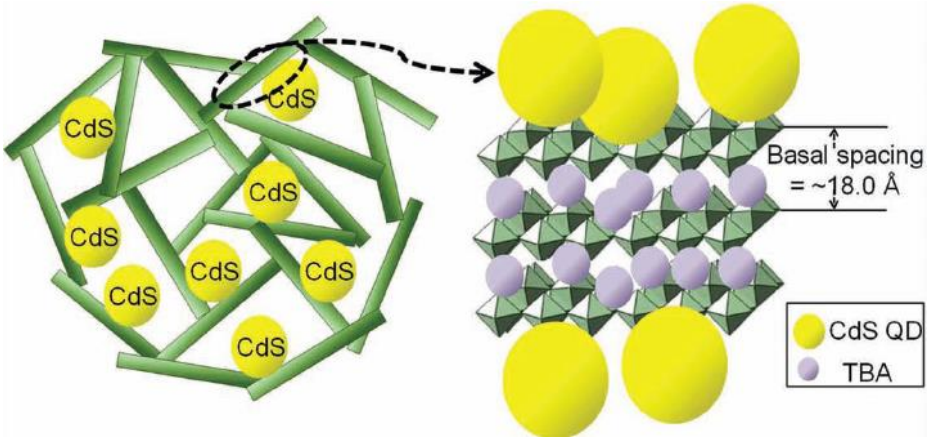

Fig. 22. Structural model of CdS QDs – layered titanate nanosheet hybrid. Reprinted with permission from Ref.[106]. Copyright 2011 WILEY-VCH Verlag GmbH & Co. KGaA, Weinheim.

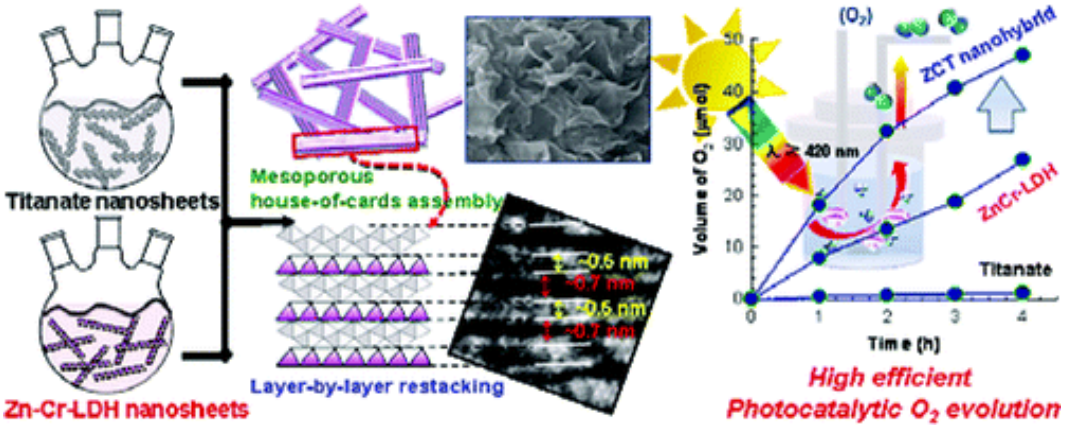

Fig. 23. Schematic process of preparing Zn-Cr-LDH and layered titanium oxide nanosheets assembly, structure of the nanosheet assembly, and photocatalytic activity for O_2 generation. Reprinted with permission from Ref.[117]. Copyright 2011 American Chemical Society.

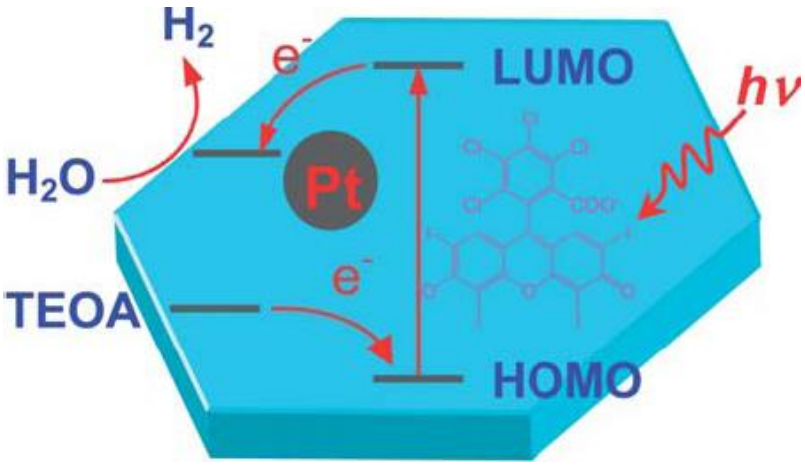

Fig. 24. Schematic diagram of photocatalytic H_2 generation on RB–LDH–Pt system. Reprinted with permission from Ref.[119]. Copyright 2011 Royal Society of Chemistry.

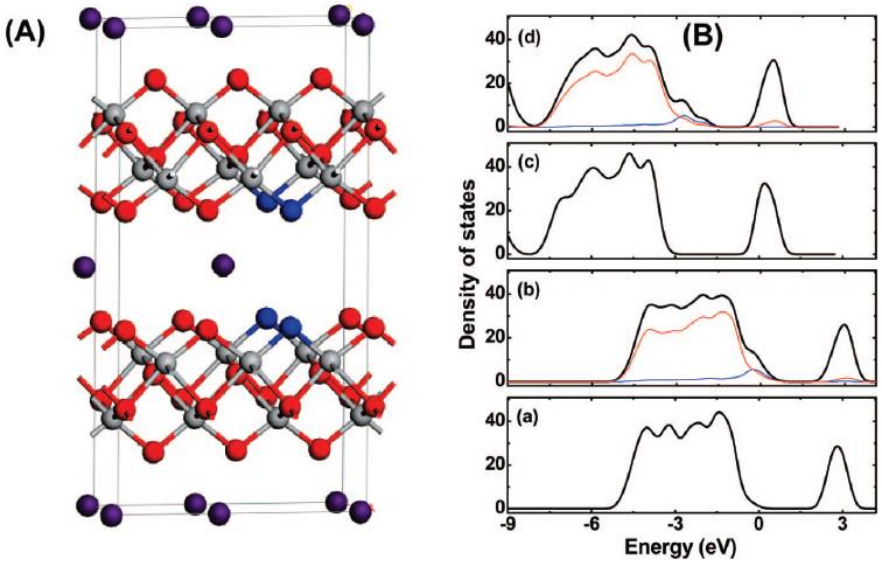

Fig. 25. (A) Structure model of cesium and protonated titanate. purple color, Cs or H; red, oxygen; gray, titanium; blue, N. (B) Total DOSs (black line) of $Cs_{0.68}Ti_{1.83}O_4$ ((a)undoped; (b) nitrogen-doped) and $H_{0.68}Ti_{1.83}O_4$ ((c)undoped; (d) nitrogen-doped) and the projected DOSs of O (red line) and doped N (blue line). The dopant N is located at a substitutional site for four O atoms in the employed models for $Cs_{0.68}Ti_{1.83}O_4$ and $H_{0.68}Ti_{1.83}O_4$crystals. Reprinted with permission from Ref.[79]. Copyright 2009 American Chemical Society.

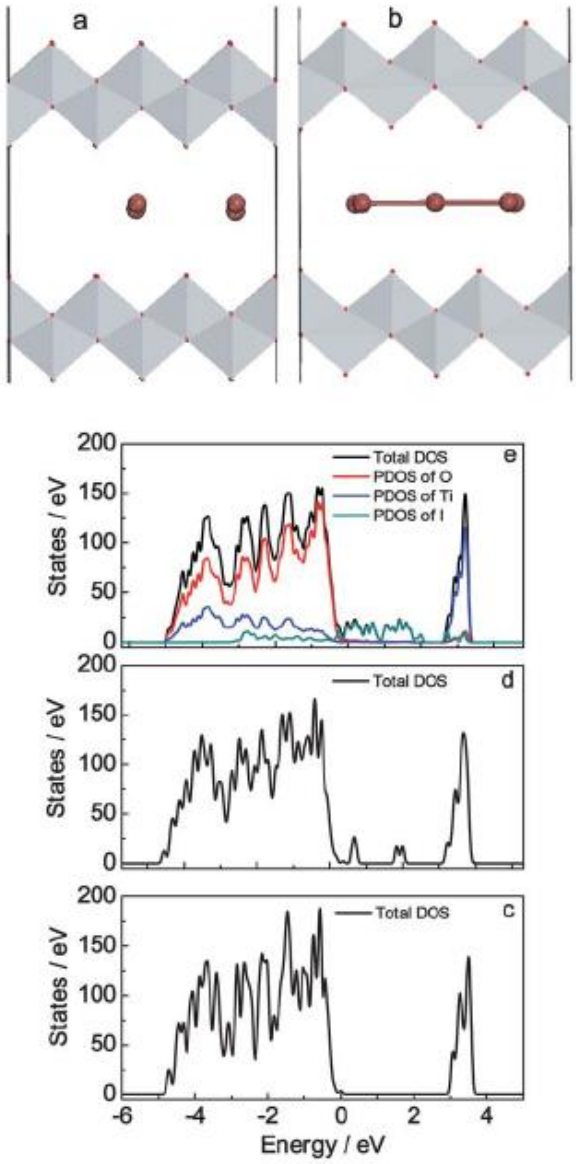

Fig. 26. Structures from DFT optimizations, with oxygen and iodine being indicated as red, white and purple spheres, titanium located at the centres of a gray TiO_6 octahedtron. (a) Adsorption of four iodine atoms on the $Ti_{0.91}O_2$ sheets; (b) Adsorption of eight iodine atoms on the $Ti_{0.91}O_2$ sheets. Calculated density of states for (c) (4 × 4) supercell of pristine $Ti_{0.91}O_2$ sheets; (d) $Ti_{0.91}O_2$ sheets with the adsorption of four iodine atoms; (e) $Ti_{0.91}O_2$ sheets with the adsorption of eight iodine atoms. Reprinted with permission from Ref.[104]. Copyright 2011 Royal Society of Chemistry.

Xu Zong received his PhD (2010) degree from the Institute of Chemical Physics, Chinese Academy of Science. He is currently a postdoctoral research fellow in the ARC Centre of Excellence for Functional Nanomaterials (ARCCFN), the University of Queensland. His research interests mainly focus on photocatalytic and photoelectrochemical water splitting using semiconductor materials, including ion-exchangeable layered materials.

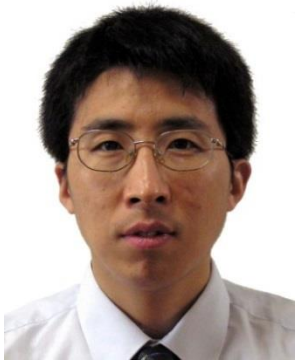

Lianzhou Wang received his PhD degree from Shanghai Institute of Ceramics, Chinese Academy of Sciences in 1999. He is currently a Professor in School of Chemical Engineering and Research Director of ARC Centre of Excellence for Functional Nanomaterials (ARCCFN), the University of Queensland. Prof. Wang's research interests include the design and development of functional nanomaterials for use in renewable energy conversion/storage systems, including photocatalysts, photoelectrodes for low cost solar cells, and rechargeable lithium ion batteries.